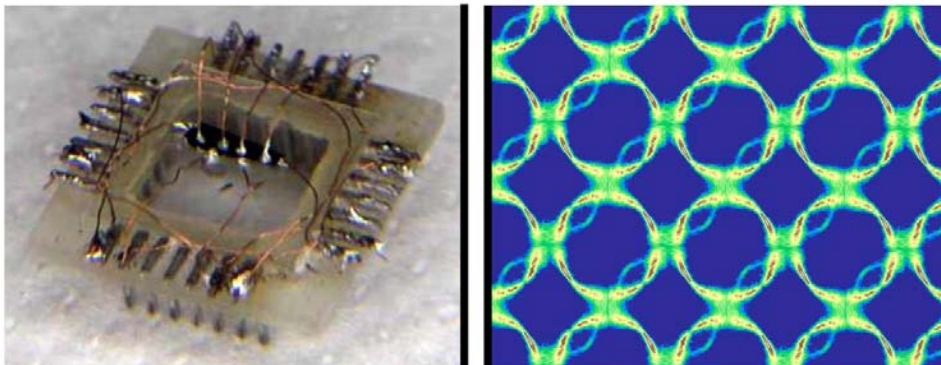# THE QUEST FOR UNDERDOPING

Resistivity and ARPES measurements on
$(Pb,Bi)_2Sr_2CaCu_2O_{8+\delta}$

Amsterdam, 3rd November 2006
Under supervision of Prof. Dr. M.S. Golden

Freek Massee

Thesis for obtaining master's degree in physics
University of Amsterdam, FNWI, Van der Waals-Zeeman Institute

The quest for underdoping

Freek Massee

3rd November 2006

Contents

6 Conclusions 66

7 Nederlandse Samenvatting 67

8 Acknowledgements 69

A Gauge Invariance 70

B Reliability of resistivity measurements 72

C Angular distortion corrector 74

D Beamtimes 75

1 Abstract

In the Master's project of which this is the thesis, resistivity and photoemission measurements were performed on $(Pb,Bi)_2Sr_2CaCu_2O_{8+\delta}$ in order to determine the effect of different annealing treatments on the hole doping concentration per Cu atom. The aim of the project was to find a treatment which would get the samples underdoped. However, it was found that the methods used so far do not lead to an underdoping of the crystals. Even annealing at $700\,^{\circ}C$ in vacuum for 24 hours does not result in samples that show clear signs of underdoping. Instead, the aggressive anneal is likely to make the samples very disordered, leading to upturns in resistivity just above the superconducting transition temperature. Anneals, all measurements and data analysis were performed by the author, unless stated otherwise.

2 Introduction

2.1 How it all began...

What would the world look like without electricity? Hard to imagine, but it is only a mere 200 years ago that Faraday, Galvani, Volta, Ampère, and Ohm laid the foundations of our modern electrical technology. A hundred years later, electrical engineering was a profession on its own, striving to develop and perfect techniques of electrical transmission. During this period of intense activity in the field of electronics, Heike Kamerlingh Onnes (figure 1) did perhaps an even more astonishing discovery than his colleagues a hundred years before.

Figure 1: Heike Kamerlingh Onnes (1853-1926), discoverer of superconductivity and awarded the Nobel prize in 1913 for his work in cryogenics.

Onnes, at the time professor at Leiden University, was founder of a cryogen-

ics laboratory and expert in the field of cryogenics. He was the first physicist to liquify helium and, using the Joule-Thomson effect managed to reach 0.9 K in the year 1908. At the time, a big discussion was going on what would happen to an electric current through a metal when it was cooled down to absolute zero. Some believed the electrons to come to a full stop, meaning no current would flow anymore. Others like Onnes believed the resistance would steadily drop down to zero resistance at absolute zero temperature. To investigate this matter, Onnes cooled several pure metals (mercury, tin and lead) in his cryostats while measuring the resistance. At 4.2 Kelvin, the resistance of mercury suddenly dropped to zero and entered a new state which Onnes called in his 1911 paper **superconductive state** (though at first he preferred the term supraconductive). After his first discovery, more and more materials were found that also become superconducting below a certain temperature, the field of superconductivity was born.

The first theories to explain superconductivity were published in the 50's and in 1957 the complete microscopic BCS theory by J. Bardeen, L.N. Cooper and J.R. Schrieffer was proposed [28]. Both types (I and II) of superconductivity could be explained by the BCS theory, so the mysterious state was finally understood. In 1979 however, a superconductor, $CeCu_2Si_2$, was found that did not conform to the BCS theory and was termed an unconventional superconductor [30]. When J.G. Bednorz and K.A. Müller found a cuprate perovskite-based material in 1986 with a transition temperature of 35 K [27], the first unconventional **high temperature superconductor** was found. BCS theory predicts transition temperatures not to exceed 30 K, so a new explanation had to be devised. Although many ideas have been put forward, none succeeds to explain all available data and convince the field of its correctness. Soon other cuprate perovskite-based materials were found with even higher transition temperatures, $YBa_2Cu_3O_{7-\delta}$ (YBCO, T_c =92K) and $Bi_2Sr_2CaCu_2O_{8+\delta}$ (Bi-2212, T_c =95K) being the most well known, with as current transition temperature record holder $(Hg_{1-x}Tl_x)Ba_2Ca_2Cu_3O_{10+\delta}$ with T_c =138K. The quest for understanding high temperature superconductors and perhaps finding a room temperature superconductor was initiated.

2.2 BCS in a nutshell

In a normal metal, electrons are scattered by lattice vibrations or defects in the structure, leading to a finite resistance of the material. Lowering the temperature of a system reduces the lattice vibrations, which in turn lowers the resistance, but due to defects there will always remain a certain residual resistance in a metal. In a superconductor the electrons somehow order in such a way that they are no longer scattered, either by lattice vibrations or defects. One of the first steps towards understanding this mechanism

was taken by L.N. Cooper, when he proposed that any attractive interaction between electrons in an electron gas, no matter how weak, would lead to pairing of the electrons, despite the Coulomb repulsion [29]. Therefore electrons, which are fermions, could form a composite boson, provided there is some sort of effective attractive interaction. This attractive interaction turned out to be mediated by lattice vibrations, or phonons. Below a certain temperature it will become energetically favorable for electrons in a superconducting material to form such Cooper pairs. The pairs can then condense in a collective ground state wave function, lowering the energy of the entire system. Since breaking up a Cooper pair affects the collective ground state wave function, an energy gap is opened. The electrons in Cooper pairs are therefore no longer scattered, but will remain in the collective ground state, resulting in zero resistivity.

BCS theory however only considers Cooper pairs with a net angular momentum of zero ($L = 0$), i.e. spherical symmetric s-wave pairs. The discovery of pairs with a finite angular momentum, mostly $L = 2$ or d-wave pairs, but also p-wave pairs, could not be explained by BCS and these superconductors were termed unconventional. The exceptionally high transition temperatures furthermore are believed by many to rule out a phonon mediated attractive interaction between the electrons. To date there is still no comprehensive theory of unconventional superconductors, although many ideas have been put forward. The next section will discuss a selection of what is known about the group of copper oxide based high temperature superconductors, which form the main body of unconventional superconductors.

2.3 High T_c superconductors

All copper oxide (cuprate) high T_c superconductors, including Bi-2212, consist of a layered structure with one or more copper oxide planes per unit cell. Figure 2 shows a unit cell of the single layered high T_c superconductor $La_{2-x}Sr_xCuO_4$ (LSCO). Band structure calculations indicate that for all copper oxide superconductors, the energy levels between the Fermi level and several eV binding energy find their origin in the copper and oxygen planes. The copper oxygen atoms generally form a tetragonal structure with a Jahn-Teller distortion in the direction of the c-axis. The undistorted cubic structure will lead to a crystal field splitting of the partial overlapping copper $3d^9$ and oxygen $2p^6$ orbitals and lift the degeneracy of the $3d^9$ level into an e_g and t_{2g} level. The Jahn-Teller distortion further splits up these two levels into the orbital levels, with as highest level $d_{x^2-y^2}$ because of its geometry relative to the distortion. Of the nine d-electrons of copper, only one will therefore occupy the $d_{x^2-y^2}$ and the level is half filled. Since the on-site electron-electron repulsion U is much larger than the band width W
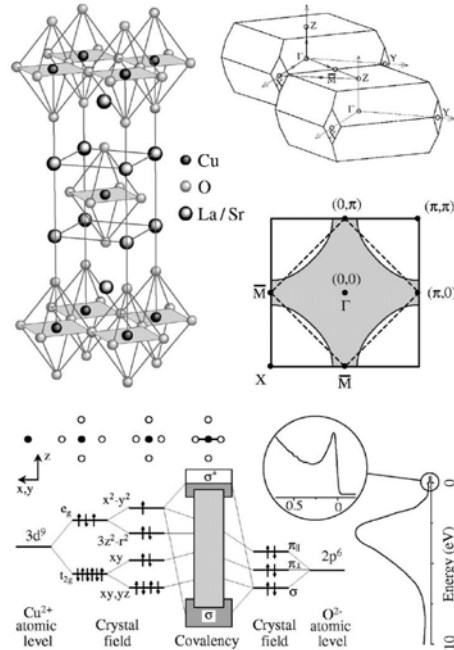
Figure 2: Layered crystal structure of $La_{2-x}Sr_xCuO_4$ (top left), with a 3D image of the first Brillouin zone and its 2D projection (top right). Energy level splitting due to tetragonal crystal field and Jahn-Teller distortion (bottom left) with generic photoemission spectrum (bottom right) [12].

of this level, there is a splitting of the band in an upper and lower Hubbard band. The undoped copper oxide superconductors are therefore antiferromagnetic Mott-insulators with an energy gap of a few eV.

Aside from the copper oxygen layers, a cuprate superconductor has one or more other layers that act as charge reservoirs. LSCO for instance has a layer of lanthanum oxide separating the copper oxygen planes. By either substitution of elements in or adding oxygen atoms to these layers, holes are introduced in the copper oxygen planes. When for instance Sr, which has a filled s-shell is substituted for La, which has a single p-electron, one electron is taken from the CuO-plane and a hole is left behind. For low hole doping concentrations, the holes are situated on the oxygen atoms in the CuO-plane and are localized in character. The material remains an antiferromagnetic insulator. When the hole doping is increased, an insulator-metal transition occurs and the material starts to conduct, although weakly. The region between antiferromagnetic insulator and superconductor has an until now mysterious **pseudogap**, a considerable drop in the density of states at the Fermi level. In the pseudogap phase, neither superconducting nor insu-

lating properties are exhibited. Above a certain temperature T^* there is a crossover to a Fermi liquid like phase where the pseudogap is closed, just like the superconducting gap is closed at T_c. Many believe that understanding this pseudogap phase is the key to understanding high T_c superconductors; is it for instance competing with, or a precursor to superconductivity?

At a doping concentration of slightly less than 0.1 holes per Cu atoms in the CuO-planes (x=0.1), superconductivity sets in. Injecting more and more holes in the CuO-planes will increase the number of superconducting Cooper-pairs, thus increase the phase coherence. However, the pairing strength decreases as can be determined by for instance critical field measurements, leading to an optimum doping concentration where T_c is highest. At the extreme overdoped side, superconductivity disappears and a Fermi liquid like metal is obtained. Figure 3 shows the phase diagram of a high temperature superconductor, where the temperature is plotted versus the hole doping concentration.
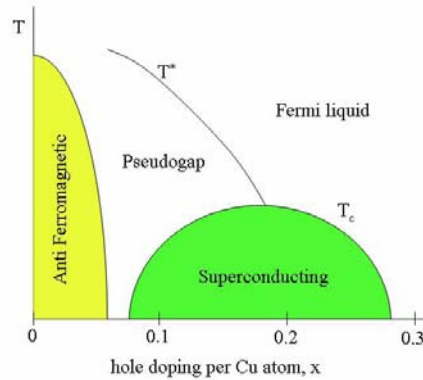

Figure 3: Schematic phase diagram of a high temperature copper oxide superconductor.

Since most properties of a cuprate superconductor seem to come from the CuO-planes, the superconductivity can be thought of as essentially two dimensional due to the relative large distances between the CuO-planes. Cuprates prove in practise to be very anisotropic, the c-axis critical current is for instance much lower than that of the ab-plane. The normal state resistivity shows a very different c-axis than ab-plane behavior (see section 4). Also the electronic dispersion along the c-axis is very weak, so in the discussion of photoemission data only the two dimensional projection of the three dimensional first Brillouin zone (figure 2) is required (see section 5.2 for further details).

3 Samples and characterization

The starting point of every experimental research is to obtain samples. All samples used in this research are made by Y. Huang at the van der Waals - Zeeman Institute in Amsterdam by the floating zone method (see section 3.1). Having samples grown by a group member inside the institute has many advantages over obtaining samples from an external source. One knows exactly what is grown and by which procedure and can discuss results directly with the grower and minor adjustments can be made accordingly. After the samples are grown they are subjected to an annealing treatment (section 3.2) and characterized by susceptibility measurements with a SQUID (section 3.4) and x-ray diffraction measurements with LAUE (section 3.3).

3.1 Floating zone technique

The floating zone method is a technique by which very pure single crystals can be grown. First, the components that constituent the eventual sample have to be put together in the proper amounts. In the case of Bi-2212 one
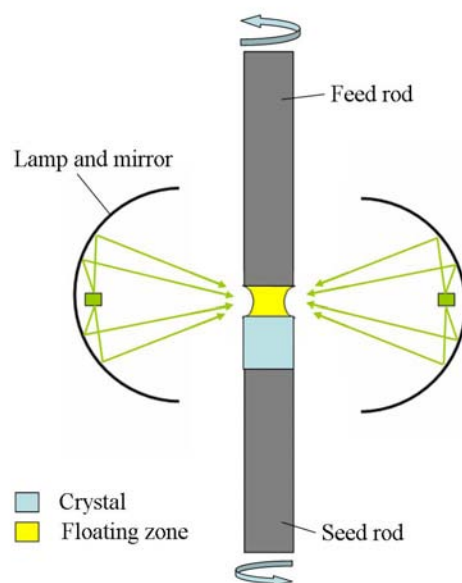

Figure 4: Floating zone method: A small part of the rod is melted by halogen lamps focused by four mirrors. Upon cooling, single crystals will form (picture adapted from W. Siu).

takes Bi_2O_3, $SrCO_3$, $CaCO_3$ and CuO as initial ingredients. These are then

weighted in the ratios of Bi:Sr:Ca:Cu = 2.1:1.9:1.0:2.0, ball milled and subjected to several heat treatments. Between each heat treatment, the powder is ground again. Eventually, the calcined powder is pressed into rods of several mm in diameter. A rod is then placed in an optical floating zone furnace (*Crystal Systems Inc.*). As can be seen in picture 4, only the part of the rod in the focal point of the mirrors is melted. After melting the central part of the rod, the top (feed) and bottom (seed) part are rotated in opposite directions to mix and the mirrors are slowly moved upwards. Single crystals will then grow in the part that is slowly cooling down below the focal point.

Bi-2212 has a periodic superstructure of approximately 5 lattice spacings (tetragonal spacings, 5.4Å) in the b-direction of the crystal. In photoemission measurements this leads to diffraction replica's of the main bands in the ΓY direction, making data analysis highly complicated. Substitution of about 20% of the Bi atoms by Pb atoms, which are a fraction smaller, turns out to suppress the superstructure. In this study, all resistivity and photoemission measurements were performed on Pb-doped Bi-2212, or (Pb,Bi)-2212 unless stated otherwise.

3.2   Annealing

The temperatures and atmospheres that are used during the growth of the crystal determines its doping concentration. To change the doping concentration, the newly grown crystal (the *as grown* crystal, or AG) can be subjected to an annealing treatment in order to add or remove oxygen from the crystal. Depending on the gas used during the anneal, the doping of the crystal will either be increased or decreased: oxygen rich atmospheres are more likely to add oxygen to the crystal and thus overdope the crystal, while for instance flowing Ar or N_2 will take oxygen that is released from the sample away, underdoping it. The temperature at which the sample is annealed is another important factor, although it is not exactly known how it affects the doping concentration. Too high temperatures, i.e. higher than $800°$C, will change the phase of the crystal, destroying its superconducting properties, while too low temperatures (lower than $300°$C) are unlikely to disturb the crystal lattice in order to effectively add or release oxygen atoms. Also the duration of the anneal is an important factor. The longer the anneal, the more homogeneous the oxygen distribution throughout the crystal. However, depending on the temperature and atmosphere it might not be possible to anneal longer than 24 hours without destroying the crystal (for instance with vacuum anneals), resulting in a more disordered crystal.

3.3 LAUE

A good method to determine if a freshly grown crystal is a single crystal and if there is any superstructure in the crystal is LAUE. It is based on the fact that crystals act as grating for x-rays, which was proposed and subsequently observed by Max von Laue (1879-1960) in 1912. The experimental setup consists of a polychromatic beam of x-rays which is directed onto the crystal and a photographic plate that detects the backscattered x-rays. Since the x-ray source is polychromatic, there will be an array of diffraction spots from the same plane, i.e. the diffraction angle will increase as the wavelength of light increases, because the lattice inter-plane distance is unaltered (see equation (46) in section 5.3). If the sample is a single crystal, only the main diffraction 'arrays' are observed, whereas in a poly-crystalline sample several single crystal diffraction patterns are observed but rotated and/or shifted with respect to each other.

As noted above, Bi-2212 has a superstructure in the b-direction of the crystal. In reciprocal space, there will thus be a scattering vector with length
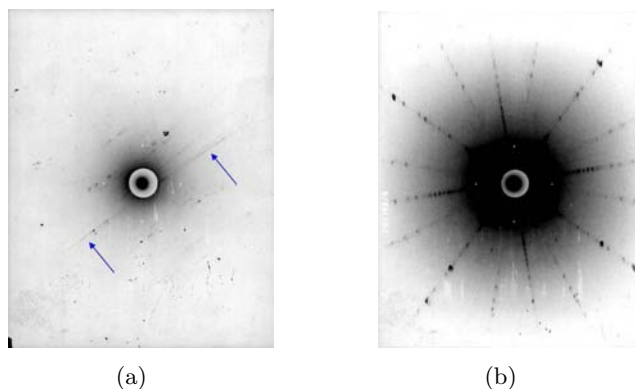

(a)   (b)

Figure 5: Comparison of a Bi-2212 crystal with (a) and without (b) super-structure. The former, non Pb-doped, clearly shows a modulation in one direction only (the b-direction) for instance at the blue arrows, although the image is of very poor quality. The latter, Pb-doped crystal, exhibits a LAUE pattern that is completely symmetric. The dark spot in the center is where the x-ray beam passes through the film. Both crystals were annealed 24 hours in vacuum at $450°C$ plus 100 hours in N_2 at $700°C$. The images are inverted for clarity.

one fifth of that from the unmodulated structure, leading to an extra array of spots in the b-direction (corresponding to ΓY in k-space). Figure 5 shows a LAUE image of a Pb-doped and non Pb-doped Bi-2212 crystal. Whereas the Pb-doped crystal is symmetric, the non Pb-doped crystal clearly shows a superstructure in one direction.

3.4   SQUID

When current flows in a circular motion, a magnetic field arises parallel to
the axis of the circular motion. Conversely, an external magnetic field in-
duces a current in a material that will counteract the field. This form of
magnetization, where a material is magnetized in the opposite direction of
the external field is called **diamagnetism**. All materials have some degree
of diamagnetic behavior, but especially conductors, i.e. materials where
electrons can freely flow through, display considerable diamagnetism. Since
in a superconductor a current can be induced without resistance, an ex-
ternal field can be completely compensated by the material[1]. Since it is
energetically favorable, all magnetic flux is expelled from a superconductor
by screening currents, even when cooled through the superconducting tran-
sition temperature in an external field (i.e. field cooling). This is called
the Meissner effect. The change of normal state to superconducting is thus
accompanied by a dramatic change in magnetization from slightly diamag-
netic or paramagnetic to perfect diamagnetic. A SQUID (Superconducting
QUantum Interference Device) can be used to measure such a change in
magnetization and thereby determine the superconducting transition tem-
perature. A typical SQUID can measure the magnetization of a material
down to $\sim 10^{-10}$ Tesla in external fields as large as 7 Teslas for temperatures
between 5K and 300K and is therefore the experimental basis of almost all
magnetization measurements.

3.4.1   Josephson effect

The SQUID is based on the *Josephson effect*, which was predicted in 1962 by
B.D. Josephson [31] (figure 6) and not much later shown experimentally.

When a thin insulating layer is sand-
wiched between two superconductors, elec-
trons can tunnel through the barrier re-
sulting in a current flow through the in-
sulator, given by

$$I = I_c \sin(\theta_L - \theta_R) \tag{1}$$

where I_c is the critical current and θ_R
and θ_L are the phases of the macroscopic
wave functions on either side of the bar-
rier. The current thus flows because of
a phase difference between the supercon-

Figure 6: British scientist Brian
David Josephson (1940-)

ducting segments. Currents below the critical current I_c, flow without dissi-
pation, i.e. they are supercurrents. This is called the D.C. Josephson effect.
For $I > I_c$ however, there is a finite voltage difference between the super-
conductors. The macroscopic wave functions of the superconductors then

---

[1]This is true as long as the external field is smaller than the critical field B_c above which
superconductivity is destroyed. For a type II superconductor flux lines can penetrate the
superconductor for fields between the lower (B_{c1}) and upper critical field (B_{c2}) without
destroying it, creating flux vortices. Only at the flux vortices superconductivity is then
destroyed.

become time dependent, i.e. the current decays like a normal current. It was found that a voltage drop $V = V_L - V_R$ leads to a time dependent phase difference $\Delta\theta(t) = \Delta\theta(0) + \frac{2eV}{\hbar}t$ and therefore a time dependent Josephson current,

$$I = I_c \sin(\Delta\theta(0) + \frac{2eV}{\hbar}t) \tag{2}$$

The current thus oscillates at a frequency $\frac{2eV}{\hbar}$. The time dependence of the current through the barrier is known as the A.C. Josephson effect.

3.4.2 Double junction

A SQUID consists of a superconducting ring with two barriers, i.e. two Josephson junctions (see figure 7) where $I < I_c$. The current is given by the
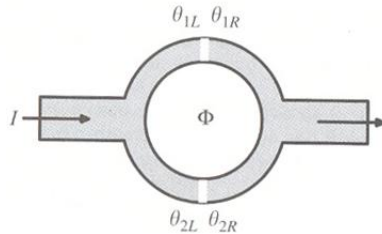

Figure 7: Schematic view of a SQUID ring. Two Josephson junctions are inserted both with their own phase difference.

sum of the two junction currents,

$$I = I_{c1} \sin(\Delta\theta_1) + I_{c2} \sin(\Delta\theta_2) \tag{3}$$

However, if there is a magnetic flux Φ present in the ring, the current flow will be altered. Without getting into the details of the calculation, the flux through the ring will induce a current to flow besides the current that is already present, leading to a modulation of the critical current, given by

$$I_c(\Phi) = I_0 |\cos(\frac{\pi\Phi}{\Phi_0})| \tag{4}$$

Figure 8 shows the modulated critical current, which has a maximum at each successive flux quantum. Since the flux quantum $\Phi_0 = \frac{h}{2e} \sim 2 \times 10^{-15} \text{Tm}^2$, and a SQUID can be made with an area approaching 1 cm^2, it is possible to measure magnetic fields below 10^{-10} Tesla. In particular changing magnetic fields are easy to measure in a SQUID. By counting the number of minima in the modulated critical current the number of flux quanta through the ring is obtained.
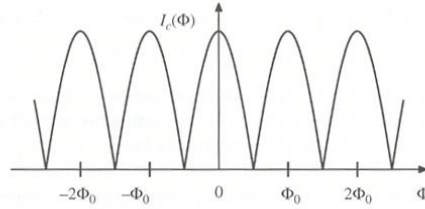
Figure 8: Modulated critical current in a SQUID ring when a flux Φ passes through the ring.

3.4.3   The device

The SQUID ring is only a small part of the actual device. Since extremely small fields are to be measured, the slightest fluctuation in the external field (including the magnetic field of the earth), could disrupt the entire measurement. Therefore a strong shielding is required from fields outside the device and the applied external field should be extremely stable. Since measurements will take place primarily at low temperatures, the sample needs to be cooled as well. Figure 9(a) shows a schematic view of a SQUID with all requirements incorporated. Several vacuum shells and a Helium bath ensure a stable temperature control of the sample area in the center of the SQUID. The outermost shell consists of a filament of superconducting wire that can produce very uniform vertical external fields up to several Tesla. The actual detection coils that pick up the changing magnetic field due to the sample movement are shown enlarged in figure 9(b). Four loops are connected in series, where the top and bottom loop are winded contra to the middle ones. With this configuration a uniform external field will have no net effect, only the sample moving through the coils will result in a net inductance of four times the inductance of a single coil. The four coils are connected to the SQUID ring which is located some distance below the sample chamber, completely shielded from any external field.

The *Quantum Design* MPMS-5S SQUID is used in this research. Samples are mounted with their c-axis parallel to the magnetic field in a plastic straw, kept into place with two halves of a plastic capsule. A tiny drop of apiezon vacuum grease is used to keep the sample in this orientation. To ensure a uniform temperature all over the sample, holes are made in the straw close to the sample.
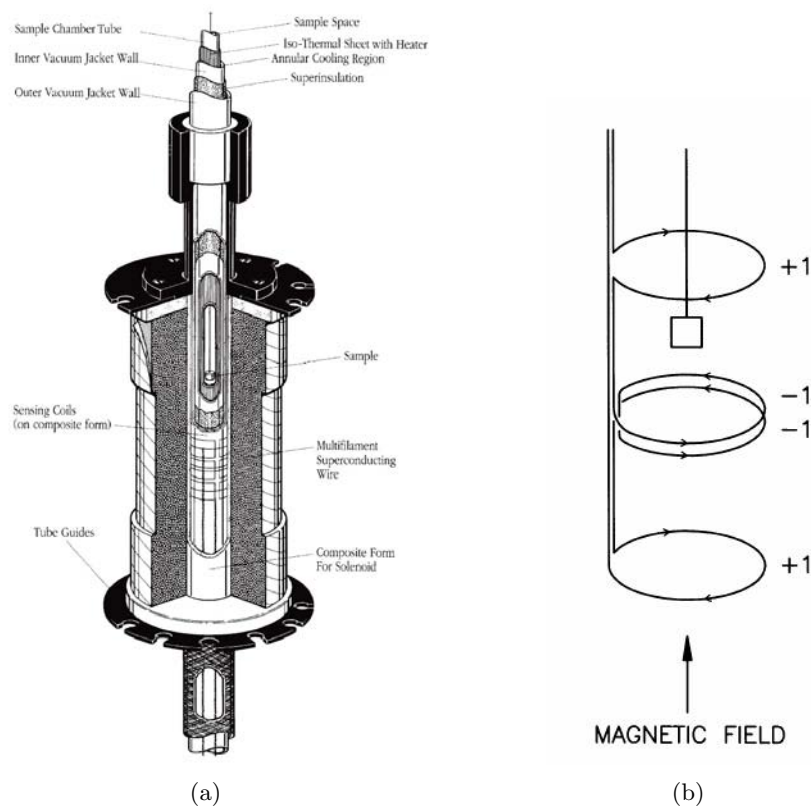
Figure 9: (a) Schematic view of the SQUID [40]. (b) Enlarged image of the detection coils [40].

3.5 Anneals and T_c's

During the project, as grown (AG) samples have been subjected to several different annealing treatments to try to obtain different doping levels. The parameters important for an anneal are the period over which, the atmosphere in which and the temperature at which the samples are annealed. Table 1 lists the different anneals and the superconducting transition temperature, determined by a susceptibility measurement of one of the samples after annealing. Figure 10 shows two typical susceptibility curves measured with an external field of 1 Gauss. The width of the transition is a reflection of the homogeneity of the sample. A short, but aggressive anneal will result in a less homogeneous crystal than a long, less aggressive anneal; the former will thus have a broader transition. The point were the susceptibility starts to drop drastically is taken as the superconducting transition temperature. Typical transition widths are several Kelvin. ARPES and resistivity measurements which have been performed on a selection of these annealed samples will be discussed in the following sections.

Anneal (time, atmosphere, temperature)	Batch	T_c (K)	Label
AG	0606	84	Q
AG	290604	84	
24h Ar 600°C	-	78	P
72h Ar 750°C	290604	86	
72h Ar 700°C	-	82	R
100h Ar 700°C	290604	82	
100h+84h Ar 700°C	290604	81	N
200h N$_2$ 700°C	290604	81	
24h Vacuum 450°C + 100h N$_2$ 700°C	30012006	80	
non Pb-doped, 24h Vacuum 450°C + 100h N$_2$ 700°C	air	80	
>12h Vacuum 450°C + 100h N$_2$ 700°C	290604	78	M
24h O$_2$ flow 600°C	290604	70	O

Table 1: Different annealing procedures with the name of the batch and T_c. Samples from different batches might have a different T_c, because the growth process is never completely reproducible.
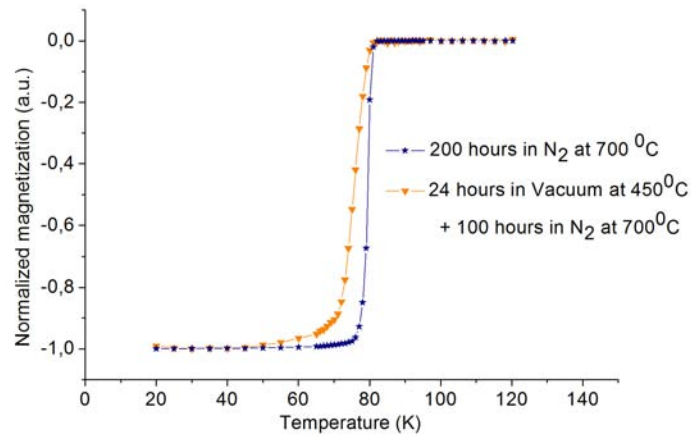

Figure 10: Two typical susceptibility measurements performed with a SQUID. The short aggressive anneal leads to inhomogeneity, as can be seen by the relatively broad transition. Data points around the transition are taken with 1 K increments.

4 Resistivity

One of the properties that make superconductors unique is zero resistance below T_c. The higher T_c of a superconductor, the worse it will conduct in its normal state as can be seen from equation (5) for the critical temperature which follows from BCS theory,

$$kT_c = 1.14\hbar\omega_D e^{-\frac{1}{V_0 Z(E_F^0)}}. \tag{5}$$

Here ω_D is the Debye frequency, V_0 gives the interaction strength between electrons and $Z(E_F^0)$ is the pair density of states at the Fermi energy. A stronger interaction between the electrons at the Fermi level gives rise to a higher T_c. The same interaction reduces the conductance in the normal state, i.e. the material has a higher resistivity. Although high T_c superconductors like Bi-2212 cannot be accurately described by standard BCS theory, they do turn out to be bad conductors above T_c. A typical value of the resistivity through the CuO-planes of optimal doped Bi-2212 at room temperature amounts to several mΩ mm, relatively high compared to 0.017 mΩ mm for copper at room temperature . Perpendicular to the CuO plane the resistivity is more than a factor 10^4 higher due to the anisotropy of the crystal.

A measurement of resistivity versus temperature is not only a precise method to determine T_c, the shape of the normal state resistivity gives accurate information on the doping of the crystal. From a measurement of T_c in a SQUID, no definite information about the doping is obtained. Since the superconducting dome in the phase diagram of a high T_c superconductor is symmetric (figure 3), for a given T_c one could be on either side of optimum doping, without knowing which side. The resistivity above T_c on either side of optimum doping is however different. At the underdoped side is the pseudogap phase, whereas at the overdoped side a Fermi liquid-like phase resides.

The resistivity of a material is caused by scattering of electrons. Scattering can be due to a number of mechanism, each of which has a material dependent strength. In good approximation, the resistivities of the individual scattering processes can be add up to give the total resistivity of a material, which is known as Matthiesen's rule:

$$\rho_{tot} = \rho_0 + \rho_{e-e} + \rho_{e-ph} + ... \tag{6}$$

where ρ_0 is due to scattering of electrons from defects, ρ_{e-e} due to electron-electron scattering, ρ_{e-ph} due to electron-phonon scattering etc.. For a simple metal like copper, for instance, electron-phonon and electron-defect scattering are predominant. Since lowering the temperature reduces the thermal activity of the lattice, the scattering of conduction electrons by

phonons becomes less and the resistivity decreases. However, since impurities are unaltered by a change in temperature, electrons will be scattered by them down to absolute zero, leading to a constant non-zero resistivity. An electron-electron contribution, which for a Fermi liquid is proportional to the square of the temperature, is for a good conductor like copper very small. For a strongly correlated electron system such as Bi-2212, however, electron-electron scattering is the predominant scattering process. As it turns out, the temperature dependence of (in-plane) resistivity of Bi-2212 is linear from extremely high temperatures (>1000K) down to the superconducting phase transition, where the resistivity drops to zero (see figure 11(a)). For normal metals, the resistivity levels off at high temperatures, when the inelastic mean free path approaches the lattice spacing. For still unexplained reasons, this Ioffe-Regel limit is exceeded by far in Bi-2212.

Insulators and semiconductors have a very different temperature dependence of resistivity. For high temperatures, the thermal energy allows some electrons to reach unoccupied states and start conducting. Decreasing the temperature reduces scattering of these electrons by phonons, but also diminishes their number. The resistivity is approximately linear down to a point where the thermal energy becomes insufficient to excite electrons into the conduction band. The resistivity starts to increase and will be infinite at zero temperature. Since there are several insulating layers between the
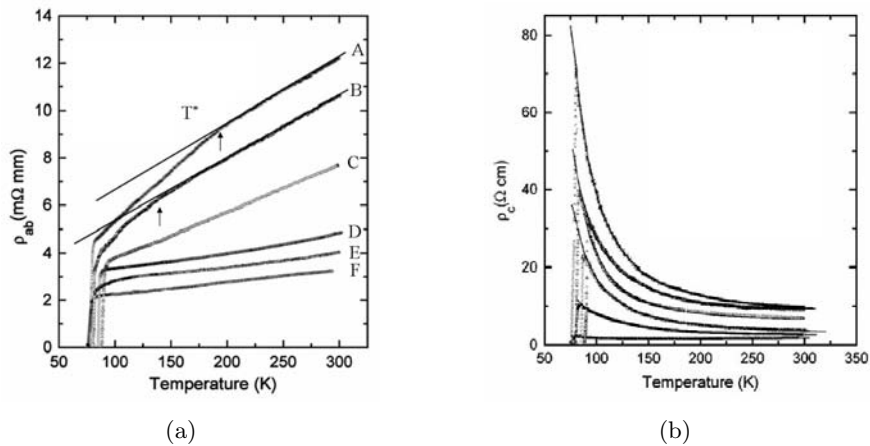

Figure 11: Literature data: (a) Temperature dependence of ab-plane resistivity of various doping concentrations of Bi-2212. For the overdoped samples (C, D, E and F) the resistivity is Fermi liquid like down to the superconducting phase transition. A clear kink can be seen at the pseudogap phase transition T* for the underdoped samples (A and B), indicated by arrows. (b) Temperature dependence of c-axis resistivity with insulating behavior. (from [15])

conducting CuO_2 planes, c-axis resistivity of Bi-2212 behaves much like an insulator. It has a much higher absolute resistivity than ab-plane resistivity and shows a distinct upturn until it becomes superconducting. Figure 11(b) shows typical curves of c-axis resistivity for different doping levels.

In the pseudogap phase, a spin-gap opens between the filled and the empty states, similar to the superconducting gap. The material however does not become superconducting, leading to the term pseudogap. It is probable that in the pseudogap phase pairs form like in a superconductor, but that the pairs are incoherent and will not form a collective ground state wave function. The phase coherence increases with increasing doping, while the pairing strength decreases, leading to an optimum doping which is approximately where the pseudogap phase transition crosses the superconducting phase transition. If a gap or partial gap opens, the resistivity can be affected in two ways: by the reduction of current carrying states, leading to an increase in resistivity, or by the reduction of scattering of carriers by electronic excitations, resulting in an decrease in resistivity. In high T_c superconductors, the reduction of scattering by spin fluctuations turns out to be the most important effect [25]. Upon crossing the pseudogap phase transition temperature (T^*), the resistivity has a clear kink in slope (see figure 11(a)). In this manner, with a fairly simple technique is it possible to determine the exact doping concentration of a sample. Moreover, the transition in resistivity between normal and superconducting state is sharper than in susceptibility, since the susceptibility is a bulk property and current needs only a single superconducting path through the sample. In practise however, making electric contact with the material turns out to be rather tricky, making the method less favorable.

4.1   Theory

In this section, several methods for measuring the resistivity of a material
will be discussed, ranging from basic two point measurements to the con-
tact resistance insensitive van der Pauw method together with theory. The
resistance of a material is defined as the ratio of voltage and current (7)
and therefore depends on the size and shape of the material.

$$R = \frac{V}{I} \tag{7}$$

This equation, known as Ohm's law, is valid for DC currents. Since all
measurements are conducted with an AC signal instead of a DC signal, the
concept of **impedance** should however be considered, which is a generaliza-
tion of Ohm's law. Measurements are performed with an AC signal instead
of a DC signal, because of the phase dependence of the AC method. In com-
bination with a lock-in amplifier noise contributions are much reduced, since
only the output signal in phase with the input signal is detected. Therefore
also a constant thermopotential, produced by the thermoelectric effect, due
to the use of materials with different absolute thermopowers (K), is elimi-
nated with an AC measurement[2].

When using an AC signal, the current becomes sinusoidal,

$$i = I \cos \omega t \tag{8}$$

where ω is the frequency of the alternating current and t the time. In case
of a resistance in an AC circuit, it can be seen from Ohm's law that the
potential also becomes a sinusoidal function, in phase with the current. For
inductors and capacitors in an AC circuit however, a time derivative shifts
the phase of the potential. Equations (9), (10) and (11) are the potential of
a resistor, inductor and capacitor in an AC circuit respectively.

$$
\begin{align}
v_R &= IR \cos \omega t \tag{9} \\
v_L &= IX_L \cos(\omega t + \frac{\pi}{2}) \tag{10} \\
v_C &= IX_C \cos(\omega t - \frac{\pi}{2}) \tag{11}
\end{align}
$$

In these equations, R is the resistance, $X_L = \omega L$ the inductive reactance
and $X_C = \frac{1}{\omega C}$ the capacitive reactance. Since the resistance and inductive
and capacitive reactance are phase dependent, they should be treated as

---

[2]A thermal potential is only nonzero if there is a temperature gradient between equiv-
alent pairs of contacts in the route to and from the source. When performing a DC
measurement, the current is commuted to determine the contribution to the resistivity
due to thermal voltages

vectors, or phasors. In an L-R-C circuit the potential then becomes the sum of the projections of the phasors $V_R = IR$, $V_L = IX_L$ and $V_C = IX_C$,

$$V = I\sqrt{R^2 + (X_L - X_C)^2} \tag{12}$$

What is actually measured in an AC circuit is therefore not the resistance, but the impedance Z, defined as the ratio of voltage amplitude across and current amplitude in the circuit,

$$Z = \sqrt{R^2 + (\omega L - 1/\omega C)^2} \tag{13}$$

which in case of a pure resistor reduces to $Z = R$. Therefore, the in-phase signal of Bi-2212 which is measured, can be treated as if it was measured in a DC circuit.

A size independent measure of the transport properties of a material is the **resistivity** which can be deduced from the resistance combined with the size and shape of a material. For simple geometries, for instance wires and rectangles, the resistivity is given by

$$\rho = \frac{RA}{l} \tag{14}$$

where R is the resistance, A the area through which the current flows and l the length of the conductor. The reciprocals of resistance and resistivity are conductance (G) and conductivity (σ) respectively.

4.1.1 Two point resistance

The standard way to check the resistance of something is the two point method. Anything ranging from a pencil to electric wirings of a building could be the focus of interest, but for this research most important is to know if the contacts on a sample are good enough to proceed with a measurement. The simplest form of a two point measurement is to connect two ends of the material to a source with a known voltage and measure the current through the circuit with an ammeter that is placed in series with the sample. Figure 12 shows a schematic view of a typical two point measurement of resistivity. Using equation (7) the resistance of the circuit can be calculated. Since the eventual current flow is a consequence of all components between the poles of the source, the measured resistance is the sum of all resistances that are connected in series (wires, sample, contact pads etc.). This method thus gives an indication of the resistance of the contacts. A different method should be used to obtain the resistance of the sample only, for instance the four point method.
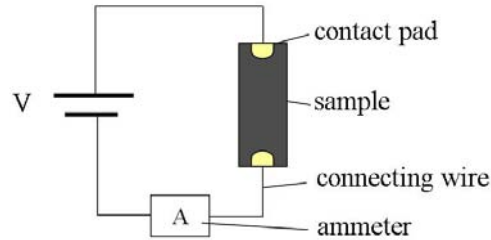
Figure 12: Typical two point measurement, showing a sample connected to a source connected by wires. The measured resistance is the sum of all components that are connected in series. The ammeters contribution is however negligible.

4.1.2   Four point resistance

There are several methods to measure the resistivity of a material, of which the four point method is one of the most used. Samples should be rod-shaped, with their a-axis long compared to the b and c axis (figure 13(a)). Four contacts are places on top of the material with equal separation between them, i.e. one third of the sample length. For the most reliable result, the

(a)   (b)
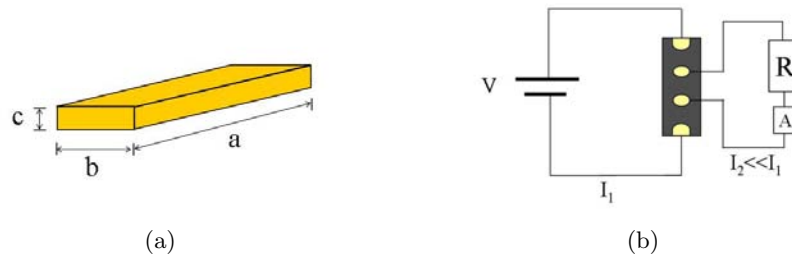
Figure 13: (a) Dimensions of a sample suitable for a four point measurement. The a axis should be much larger than the b and c axis to ensure a uniform current through the sample. (b) Schematic view of a four point setup. The current through the high resistance and ammeter is negligible, so the voltage drop is due to the sample only.

contacts should be as small as possible. A current is passed through the outer contacts, ensuring a uniform potential distribution through the sample at the voltage contacts. The voltage drop between the inner contacts can then be measured, which combined with the current gives the resistance. Taking the shape and size of the material in account, the resistivity of the material can be deduced. To measure the voltage drop between the inner two contacts, an ammeter in series with a known high resistance is connected to the contacts.

Figure 13(b) shows a schematic view of such a setup. The high resistance which is placed in series with the ammeter ensures that the original circuit is barely disturbed and almost no current flows through the contacts, high resistance and ammeter. Therefore, the measured voltage drop is in very good approximation only due to the sample. The only prerequisite is that the contacts are Ohmic, which means that they have a linear I vs V curve.

4.1.3 Van der Pauw method

The four point method is only suited to measure the resistivity of a certain sample geometry. A more general method for measuring the resistance of samples with arbitrary shape and size was reported in 1958 by Philips researcher L.J. van der Pauw. The sample should be flat, completely free of holes and provided with four small contacts at arbitrary places on the periphery. Figure 14(a) shows such a sample with four contacts N, M, O and P. One measures the potential difference between P and O (V_P-V_O) and defines the 'resistance'

$$R_{MN,OP} = \frac{V_P - V_O}{I_{MN}} \qquad (15)$$

where I_{MN} is the current through M and N. Analogous, the potential difference between P and M give a 'resistance'

$$R_{NO,PM} = \frac{V_M - V_P}{I_{NO}} \qquad (16)$$

Van der Pauw showed that between $R_{MN,OP}$ and $R_{NO,PM}$ there exists the simple relation

$$e^{-\frac{\pi d}{\rho} R_{MN,OP}} + e^{-\frac{\pi d}{\rho} R_{NO,PM}} = 1 \qquad (17)$$

with d the thickness of the sample and ρ the resistivity of the material. To determine the actual resistivity it is necessary to perform two measurements, one for each 'resistance'.

When the sample possesses a line of symmetry however, only one measurement will suffice, since both 'resistances' will be identical. In general interchange of current and voltage contacts gives the same 'resistance' and from symmetry it then follows that $R_{MN,OP} = R_{NO,PM}$ (see figure 14(b)). The resistivity is then given by

$$\rho = \frac{\pi d}{\ln 2} R_{MN,OP} \qquad (18)$$

For samples without such a line of symmetry the resistivity can be found from the following relation

$$\rho = \frac{\pi d}{\ln 2} \frac{R_{MN,OP} + R_{NO,PM}}{2} f \qquad (19)$$
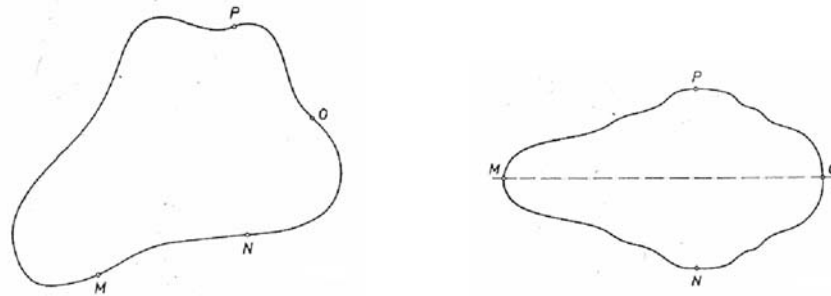
(a) A lamella of arbitrary shape with four contacts M, N, O and P.

(b) A lamella with a line of symmetry. Two contacts are placed on the line of symmetry, the other two symmetrical with respect to this line.

Figure 14: Two possible sample geometries on which the van der Pauw method of measuring resistivity is valid [6].

where f is a function of the ratio between the two 'resistances' and can be found in van der Pauw's paper [6].

4.1.4   Montgomery method

To determine the resistivity of a material in a certain crystallographic direction, a method based on the results of van der Pauw is used, called the Montgomery method [7]. Especially for highly anisotropic materials such as Bi-2212 the method is very powerful, for instance to compare ab-plane with c-axis resistivity. The method considers a rectangular prism with edges in the principle crystal directions. Four small contacts are placed on the corners of the edges in the directions of the two resistivity components to be measured. From two measurements and the dimensions of the sample, two components of the resistivity tensor can be calculated. The dimensions of the face in question are l'_1 and l'_2, the third dimension, or thickness, is l'_3. For a certain voltage difference over one side of the crystal with dimension l'_1 the current is measured between contacts of the opposite side. The ratio of voltage to current is then the resistance R_1. A similar measurement is subsequently made with all connections rotated by 90° to obtain R_2.

The idea of the method is that the voltage-current relation for a certain rectangular prism of an anisotropic material is mapped onto an equivalent isotropic material with different dimensions, based on the van der Pauw method [6]. The bulk resistivity of the rectangular isotropic material thus obtained can be calculated using the work of Logan et al. [8], which can be expressed as

$$\rho = HER_1 \tag{20}$$

where H is a function of l_2/l_1 and E is the effective thickness. Since E and H depend on the *isotropic* dimensions, the anisotropic dimensions first have to be transformed using the voltage-current relations. The measured voltage-current ratio R_1 and R_2 of the anisotropic material would by definition also be observed on the equivalent isotropic material. Knowing the ratio R_2/R_1, the dimensions of the isotropic solid can be found from Logan et al.. A simple transformation of coordinates by Wasscher [9], based on van der Pauw's work, is then given by

$$l_i \quad = l_i' \sqrt{\frac{\rho_i}{\rho}} \tag{21}$$

$$\rho^3 \quad = \rho_1 \rho_2 \rho_3 \tag{22}$$

which combine to

$$\sqrt{\frac{\rho_1}{\rho_2}} = \frac{l_2}{l_1} \cdot \frac{l_1'}{l_2'} \tag{23}$$

where l_i and ρ_i are the dimensions and corresponding resistances respectively of the isotropic solid. Assuming a thin sample, $l_3 << \sqrt{l_1 l_2}$, E is equal to l_3. Rewriting equation (21) one obtains

$$l_3 = l_3' \left(\frac{\rho_3}{\sqrt{\rho_1 \rho_2}}\right)^{\frac{1}{3}} \tag{24}$$

which, combined with equation (20) and (22), leads to the following simplified expression for the resistivity

$$\sqrt{\rho_1 \rho_2} = H l_3' R_1 \tag{25}$$

The two components of the resistivity tensor are then easily calculated using equation (23). If the sample is not thin, but the thickness has to be taken into account, matters are less simple. However, since in this research thin samples are used and the contacts are extended along the edges normal to the plane of measurement[3], the approximation holds and the thickness dependence will not be discussed.

4.2 MagLab

The MagLab (*Oxford Instruments*) is an instrument that can measure the resistance as a function of temperature and external field. Vacuum shells, a nitrogen shell, helium bath and heating element provide a stable and controllable sample-space temperature down to 5 K and over 300 K. The MagLab system has two temperature sensors, one close to the heating element and one close to the sample. The temperature is controlled by the former, while

---

[3]By extending the contacts over the entire edge, the sample becomes infinitely small. Even for physically thick samples this procedure ensures the approximation $l_3 << \sqrt{l_1 l_2}$ holds.
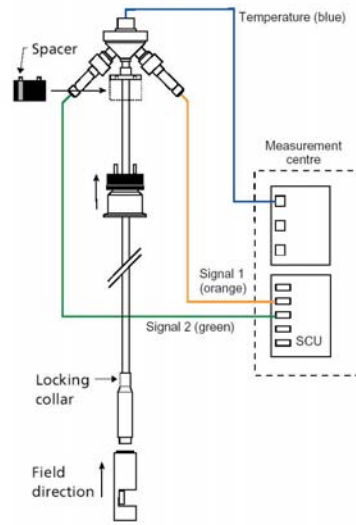
Figure 15: (Schematic image of the probe used for resistivity measurements in the MagLab. A different cabling enables the user to probe a different side of the sample holder [41].

the latter is taken as sample temperature. When the sample space is cooled or heated fast, there will be a temperature gradient between the two sensors, reaching values of more than 50 degrees. The temperature of the sample will then be somewhere in between the two sensor temperatures. For a proper measurement, the temperature gradient should therefore be as small as possible, so heating or cooling will have to be very slow. Since heating with a needle valve for the cryogen and a heating element is more controllable than cooling with just a needle valve, a typical measurement consists of the following steps:

1. fast cooling at 4 Kmin^{-1} to about 50 K; the sample temperature is not well defined, but the shape of the curve is obtained

2. slow warming at 0.5 Kmin^{-1} to room temperature; such a measurement will take more than 8 hours and is usually done overnight.

A measurement at a single current, frequency and temperature range will therefore take a full day, during which the sample contacts and the system should be stable. This requirement was unfortunately not always met. A sample is measured simply by passing a current through two contacts and reading off the voltage difference between two other contacts. With different orientations of the contacts either a Hall- or resistivity measurement is obtained. The sample holder of the MagLab has four sides, each onto which four contacts can be placed, enabling four measurements on one sample

holder without having to remove the probe from the system. By changing the cabling of the probe, a connection to different side of the sample holder is made. Figure 15 shows a schematic view of the sample probe used for resistivity measurements.

Since in this work no external field is required, a simpler setup that measures only the resistivity as function of temperature might also be used. However, the setup present in the research institute could only go down to liquid nitrogen temperatures, which is not sufficient for most samples. So although the setup itself is much less of a 'black box' than the MagLab and available at all times, few measurements have been performed on this setup.

To check if the MagLab works properly and if possible artifacts are due to the sample or to the setup, a measurement of a well known material was carried out. A copper wire in which several windings are made with an effective length of 105 mm and a diameter of 90 μm was soldered to the sample holder (see inset figure 16). Figure (16) shows the temperature dependence of the copper wire with the four point resistance on the left axis and calculated resistivity on the right axis. At room temperature (293 K) the calculated
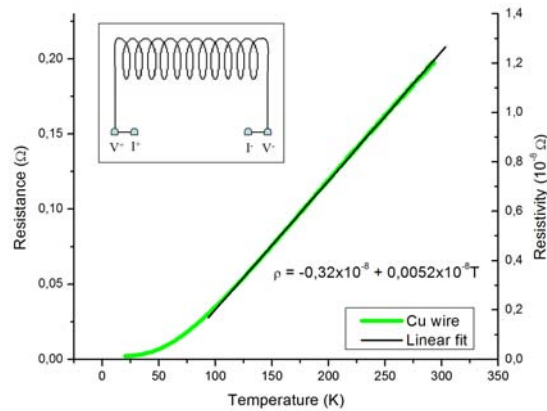

Figure 16: Temperature dependence of resistance and resistivity of a copper wire to test MagLab system, with a schematic image of the setup in the inset. A linear fit through the resistivity is shown from which the temperature coefficient is calculated.

resistivity is $\sim 1.2 \cdot 10^{-8}$ Ωm and from the fit a temperature coefficient of approximately 0.0043 can be found. For comparison, the literature values of resistivity and temperature coefficient of copper at room temperature are $1.7 \cdot 10^{-8}$ Ωm and 0.0039 respectively [37], where the temperature coefficient

is the relative change in resistivity when the temperature is changed by one Kelvin. The purity of a material has, because of electron-defect scattering, a large influence on the absolute value of resistivity and therefore also on the temperature coefficient. This might explain the difference between the measured resistivity and the literature values. The error in the length of the wire can also account for part of the difference. However, the measured absolute value of resistivity and the temperature coefficient are on the order of magnitude of literature values, which is an indication that the system operated properly during this measurement. Therefore, it can be assumed that any unexpected or unwanted result will be due to the sample and/or its contacts.

4.3   Making contacts on BSCCO...

What started as a survey of determining the effect of different annealing treatments on Bi-2212, turned out to become a struggle to make proper electrical contact with it. The most important and at the same time most difficult task is to make electrical contact with a Bi-2212 single crystal without destroying the crystal structure and its properties. A contact should be stable in the temperature range of the measurement (20K-300K) and have a long lifetime (years if possible, but at least weeks). Moreover, the contact should be ohmic, i.e. the current should increase linear with voltage, corresponding to equation (7).

According to literature, there are many different methods to make proper contacts on Bi-2212. During this research however, every method that was tried turned out to have one or more shortcomings. Therefore this chapter will be devoted to the problems of making contacts and the different methods tried so far.

One of the major problems of Bi-2212 is, that it is extremely fragile, pressing gently on it with a pair of tweezers will destroy the structure already. Therefore any method which uses some form of force onto the sample surface can be discarded, for instance simply pressing contacts onto the sample, like copper springs or razor blades. Soldering contacts directly on top of the sample surface turned out to be unsuitable as well, at least with the equipment available. For the solder to stick, the surface should be at least at the melting temperature of the solder. In order not to alter the properties of the sample, low temperature solder (70 °C) will have to be used. Also, very small contacts are required which are very difficult to make with regular soldering equipment. With more specialized equipment this problem may be solved, but even then it will be tough to make a stable connection to a flat and shiny Bi-2212 surface. The conclusion was that other methods will have to be found.

4.3.1   Silver paint

By far the largest number of groups who do resistivity measurements on Bi-2212 use some form of silver paint. It has a low resistance when dry and adheres reasonably well. The easiest method of making contacts is by painting a copper wire directly on top of a crystal. Because the typical sample size is on the order of a millimeter by a millimeter, a microscope, steady hands and patience are required to make the contacts as small as possible and clearly separated from each other. Tiny droplets of silver paint are placed onto the sample and a 10 μm copper connecting wire. Since the silver paint wets very well, the droplets should be as small as possible. A too big drop will wet the entire sample after which the crystal will have to be cleaned and the whole process can start from the beginning.

The connecting wires always experience some internal strain that tends to pull the wire from the crystal. Many times when cooling to tens of Kelvins, this strain becomes stronger than the adherence of silver paint to Bi-2212, and contact with the sample is lost.

Also, silver paint will form an insulating oxide which will lead to a deterioration of the contacts over time. Contact resistances become a factor of ten or more worse in the time span of a week. Moreover, oxide can form at the boundary of the silver paint with Bi-2212, taking oxygen from the Bi-2212 crystal. This process is speeded up when a measurement is performed: a current through the contacts will heat them, resulting in faster oxidation, thereby worsening the contacts which will produce even more heat. In a matter of minutes, the contact resistance can go from Ohms to mega Ohms.

Despite these problems, a number of measurements were performed. The absence of an out of phase signal over the course of the entire measurement is a strong indication that the contacts are in order and do not influence the measurement. These data will be discussed in detail in section 4.4.

4.3.2   Evaporated contacts

A different method to make contacts is by evaporating a conducting material on top of the sample. The evaporated pads can subsequently be connected to the sample holder by for instance copper wires and silver paint. The advantage of this method is that the evaporated material is in direct contact with the sample and well attached to it. Oxidation will cease to be a problem as well, since evaporation takes place in vacuum ($\sim 2 \cdot 10^{-5}$ mbar) and a non-oxidizing capping layer can be applied.

It was chosen to evaporate first a thin layer of chromium on a sample which

was cleaved in air before insertion. Chromium tends to stick well to surfaces, while remaining a sufficiently good conductor, making it an ideal material as connecting layer. On top of the chromium layer, a thick layer of gold is evaporated. Since gold doesn't oxidize and is a very good conductor it should, together with the chromium layer, result in stable and low resistance contact pads on Bi-2212.

Since the chance of losing contact still exists when using copper wires to connect the pads to the sample holder, a different idea was put forward. Instead of using wires, the evaporated chromium and gold film is extended to the edges of the glass plate on which the sample is mounted and contacted there by pressed contacts. Unfortunately, the evaporated film is almost never thick enough to bridge the distance between sample edges and glass substrate. A solution to this problem is to fill the gaps with silver paint. The contact between the gold film and silver paint is good and the silver won't oxidize at the gold surface boundary like it does at the Bi-2212 boundary.

For the above mentioned scheme to work, the MagLab sample holder had to be adjusted slightly. Press contacts had to be mounted on the corners of the sample holder and glass substrates had to be cut by hand.[4] Figure 17 shows the MagLab sample holder before and after the adjustments are made.

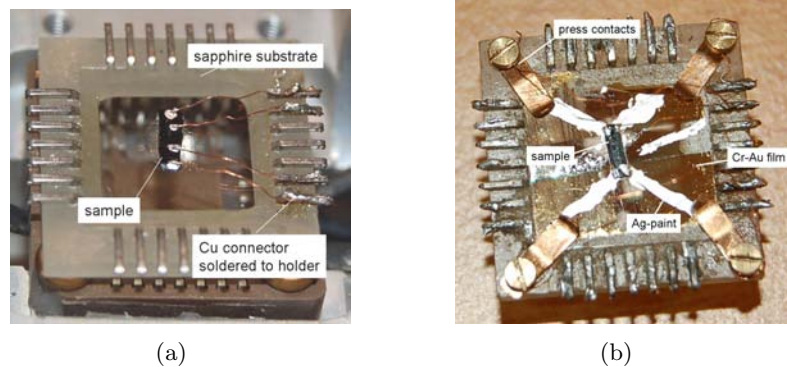(a)   (b)

Figure 17: Original (a) and adjusted (b) MagLab sample holder, with an example of a typical sample mounted on them. The press contacts are made of beryllium-copper (CuBe).

---

[4]The original sample holder has a sapphire substrate which is intended for use in all measurements. Since mounting a sample using glue makes the substrate unusable afterwards, less expensive glass (from microscope cover glasses) is cut to the proper size. Heat conduction of glass is less, but still acceptable.

4.4   Discussion of resistivity results

The pseudogap region in underdoped Bi-2212 is of special interest, since it could contain information on the interactions that are responsible for superconductivity in high T_c superconductors. Therefore it is important to be able to prepare samples in such a way that they are underdoped with a controllable doping concentration. Reducing anneals are the most used procedure to reduce the doping concentration. If this doesn't lead to the required result, substitution of atoms could be tried combined with post annealing. The latter option however requires a lot of effort from the crystal grower and is usually tried as last resort.

The aim of this research was to try different annealing procedures and determine if the annealed sample has a kink in resistivity pointing to a transition to the pseudogap phase. However, since it turned out to be less simple as expected to make electric contact with Bi-2212, the project shifted more to make proper contacts than to do systematic resistivity studies. Many measurements have been performed though, some of which under ideal conditions, on different samples. The longed-for kink in the resistivity, however, never appeared in any of the samples.

4.4.1   As Grown

Figure 18(a) shows typical measurements[5] on two AG samples with proper contact separation, such that the c-axis contribution is negligible (see section 4.4.2). Sample AG 1 had, however, considerable out-of-phase signal. Both samples have a linear resistivity as a function of temperature. Sample AG 1 has moreover a clear downturn at 101 K marked by the arrow. Instead of a pseudogap opening up however, this is caused by a small fraction of 2223-phase which has an optimum doped transition temperature of 108 K. Since no full superconducting path can be found between the two current contacts, there is only a drop in resistivity and no full superconductivity. Sample AG 2 from the same batch does not have a 2223-phase contribution and is linear down to the transition temperature. As can be seen, there is a considerable compositional variation between samples from a single batch. The transition temperatures of these two samples, which were measured under the same conditions, are 82 K and 77K respectively for sample AG 1 and AG 2.

Another interesting observation is the difference between the two measurements of AG 2 under the same conditions. The highest curve was measured a few days after the lowest curve with half of the current applied, all other

---

[5]The exact dimensions of the two samples are not known, therefore the absolute value of resistivity is a mere indication. The error is however on the order of a few mΩmm.

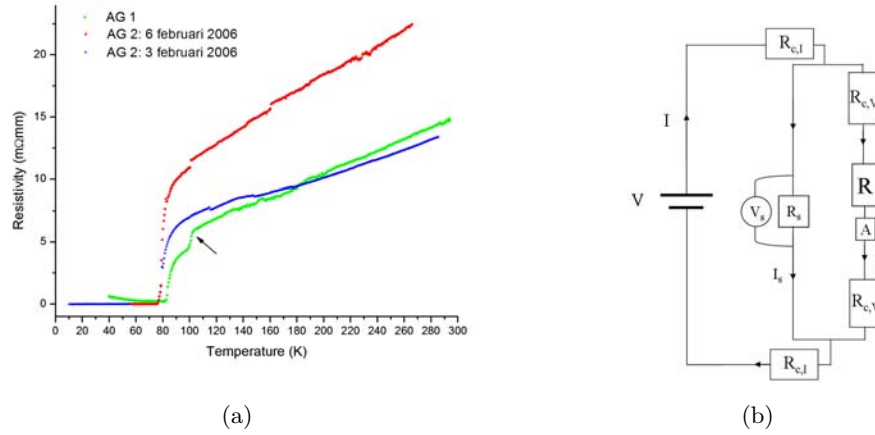(a)   (b)

Figure 18: (a) Typical temperature dependencies of resistivity of two as grown samples. Sample AG 1 has a small fraction of 2223-phase leading to a drop in resistivity at 101 K. Deterioration of the contacts leads to an increase in resistivity of sample AG 2. (b) Schematic view of measurement setup. V is chosen such that a current I flows through the sample. The potential over the sample and the parallel connected circuit are identical and is deduced by measuring the current i through the parallel circuit ($V_s = iR$ if $R_c << R$).

parameters the same. The shape is similar, but the resistivity values in the measurement taken last are however 1.8 times the first. If the contacts would not be Ohmic, it is expected that a higher current would lead to a higher contact resistance. Figure 18(b) shows a schematic view of the system with which the sample is measured. If for a certain current the voltage contact resistances ($R_{c,V}$) would be comparable to the high resistance (R) switched in series with the ammeter (A), their contribution to the measured resistivity is no longer negligible. The current (i) that will flow through the loop that measures the voltage over the sample and the resulting deduced sample resistance will be lower than it would be for negligible voltage contact resistances. So over time the contacts have deteriorated and either become non-Ohmic or simply too high resistances. Contribution from contact resistances are already apparent if for regular measurement-currents (1 mA) there is a lot of noise, indicating that i is too small. At a certain point the current contact resistances $R_{c,I}$ might even become so high, that it is not possible anymore to let a current flow through the sample at all.

4.4.2 750°C argon 72 hours

Instead of the linear temperature dependence of resistivity as shown in the previous section, many times a distinct upturn just above T_c was observed.

Since the c-axis resistivity behaves differently from ab-plane resistivity and has a clear upturn, it was at first thought that a component of c-axis resistivity was picked up to the placing the electric contacts on top of the sample instead of at the sides. For instance a dirty top layer or a crack therein would force the current to flow perpendicular to the ab-plane.

To test this assumption, eight contacts were placed on a single sample, four on the sides and four on top. By connecting the contacts to the sample holder as shown in figure 19(a), four different geometries could be measured without taking the sample out of the MagLab. An image of the sample

(a)   (b)
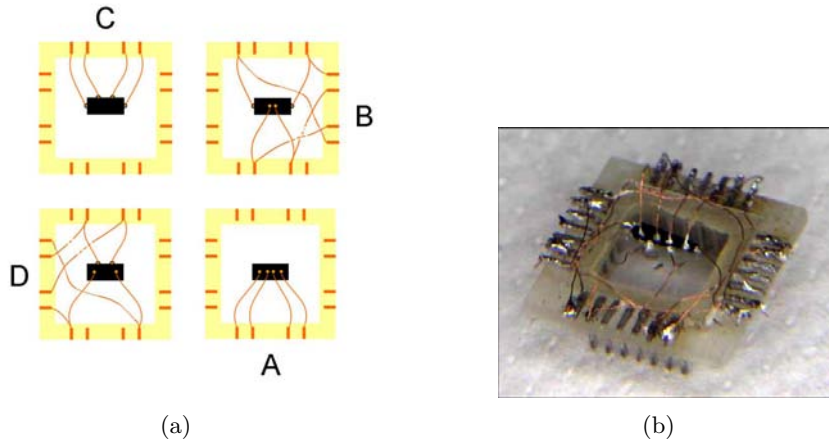
Figure 19: (a) Schematic image of the four contacts configurations to compare two methods of making electrical contact. The actual result is shown in (b).

mounted on the sample holder is shown in figure 19(b). The contacts are separated from each other and none of the connecting wires are short circuiting. Contacts resistances were relatively high compared to literature, 100 Ω compared to 1 Ω, but Ohmic. Furthermore, no out-of-phase signal was detected during any of the measurements of the sample. An ac-current is applied over the sample and the in-phase voltage over the sample is measured with a lock-in amplifier. If the system has for instance a capacitance, the signal would be phase-shifted and frequency dependent. A capacitance could for instance arise when there is an insulating layer between the sample and the contact due to oxidation. Since the presence of considerable capacitive contributions, whatever their cause, will influence the measurement, only measurements with no or negligible out-of-phase signal should be trusted. Figure 20 shows the resistivity curves for the four different orientations indicated by A-D in figure 19(a). To calculate the resistivity from the measured resistances, the thickness and width of the sample are and
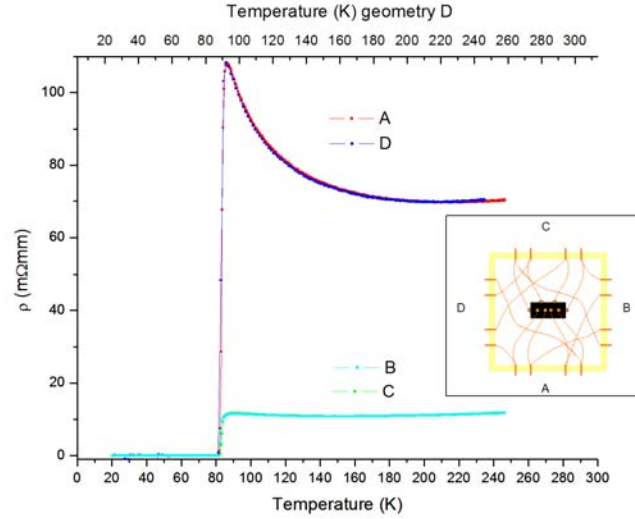
Figure 20: Plot of the resistivity versus temperature for the four different contact configurations as shown in the inset and fig 19(a). The sample is post annealed for 72 hours in an oxygen reducing Argon atmosphere at 750°C. Geometry D is measured during cooling, leading to a temperature gradient of about 3,5 K between the sample and thermometer close to the sample.

the distance between the voltage contacts are required. First of all, *none* of the four geometries show a pseudogap behavior, even though with the reducing annealing treatment this might be expected. As can be seen, the inner (voltage) contacts make no difference for the shape and absolute value of resistivity. The outer (current) contacts however have a profound impact on the resistivity. The absolute value of the contacts on top is a factor of 10 higher and whereas the side contacts show only a minor upturn, the contacts on top have a sharp c-axis like upturn.

The large difference between side and top current contacts might be explained by c-axis contribution due to a nonuniform potential distribution over the sample in case of contacts on top. The current flows perpendicular to equipotential planes. In the case of current contacts on the side, the equipotential planes are parallel to the face onto which the side contacts are placed, leading to a current along the length of the sample, along the CuO_2 planes (figure 21(a)). However, when the contacts are placed on top of the sample, the equipotential planes might not be parallel to the sides, but in a somewhat curved arrangement. The current will then have to go
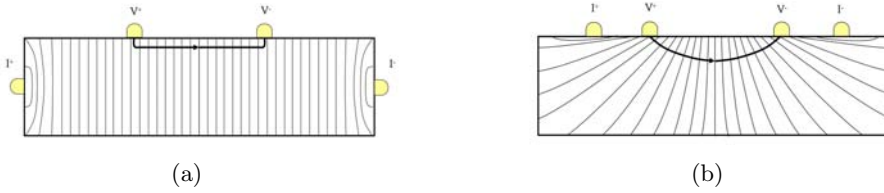
Figure 21: Schematic image of the equipotential planes and resulting current with side (a) and top (b) voltage contacts. For the latter configuration the current will go through the layers.

through the layers, leading to a c-axis resistivity component (figure 21(b)). Because of the curved path the current is forced in, top or side voltage contacts should give identical results as is indeed observed.

The c-axis contribution can be estimated by taking literature values for the ratio ρ_c/ρ_{ab}, which is at room temperature almost doping independent, and compare it to the measured ratio [15]. Thereby the assumption is made that the measurement with current contacts on the side is pure ab-plane resistivity. In doing so, about 0.07% percent turns out to be c-axis resistivity, which is as expected in percentage not much, but considerable due to the very large anisotropy. Since only a tiny c-axis contribution will thus mask a downturn due to a pseudogap, the current should be completely free of c-axis contribution. To make sure no c-axis resistivity component is measured, contacts should therefore be either far apart or on the side of the crystal. Evaporating contacts on edges cut under an angle should therefore in principle be ideal, i.e. stability of the contacts over time and no c-axis contribution.

4.4.3   450°C vacuum 24 hours

Since neither the AG samples nor the sample annealed in argon atmosphere showed any signs of underdoping, an anneal at 450°C in vacuum was initiated for 24 hours. Such an anneal is strong enough to make the sample dull and greenish, i.e. change the structure of the crystal. Therefore, if underdoping can be achieved by annealing, this vacuum anneal should be able to do it. After cleaving away the dull top layer, contacts were evaporated and several samples were measured. Again, none showed a downturn pointing to a pseudogap opening up. Yet with evaporated contacts on the sides of the sample, which were cut under an angle, an upturn in resistivity is observed (see figure 42 in appendix B). The out-of-phase signal was zero over the entire temperature range of both measurements and the contacts were Ohmic with acceptable contact resistances (60 Ohm). The measurements were performed with a low current (0,1 mA) and there was barely noise in

the signal. Therefore, the measurements are expected to be real and not caused by other factors than the sample.

Surprisingly, there is a factor hundred difference in resistance between the two Montgomery geometries, while with an approximately square sample both should give approximately the same value. Even more surprising is that the geometry with the highest resistance does not even become super-conducting. There is a downturn at the superconducting phase transition, but before reaching zero, the resistance goes up again. Increase of resistance upon decreasing temperature is typical behavior for a semiconductor. The upturn below T_c is observed twice on the sample, but never on a different sample.

A striking fact is that for measurements of at least four other samples there is a big difference of about a factor of hundred between the resistances of the two geometries. Moreover, all "high resistance" measurements were measured with the same cabling and none showed explicit signs of bad contacts for only the high resistance geometry. Therefore it is very likely that the absolute value is not due to the sample at all, but an artifact of the wiring inside the MagLab. See appendix B for more details and tests on the MagLab system, which seem to confirm this.

The upturn in resistivity might be caused by considerable disorder in the material. Studies have shown [16] that exposure of high T_c superconduc-tors to high energy electrons (2,5 MeV) introduces defects into the crystal lattice which in turn increases the absolute value of resistivity and leads to an upturn in resistivity at low temperatures. The absolute value of resis-tivity also increases upon introducing disorder into the system. The very aggressive vacuum anneal could very likely make the sample disordered and change the properties considerably yet unevenly throughout the sample. Whether the anneal is aggressive enough to make part of the sample non-superconducting but insulating is doubtful. Yet this latter could explain the upturn at low temperatures for one geometry. The fact that one geometry is superconducting and the other is not, could be caused by the absence of a contact-to-contact superconducting path in the latter case, while there is in the first case.

4.4.4   700°C nitrogen 200 hours

A very short and aggressive anneal such as described in the previous section might introduce a lot of disorder in the system and cause an upturn in resistivity. To test this hypothesis, several samples were annealed at 700°C in nitrogen for 200 hours. The long anneal will guarantee that the sample is uniform and has as little disorder as possible. Due to problems with

calculating the resistance from two separate measurements as mentioned in appendix B and inconsistent measurements probably due to a bad contact, no profound conclusions could be drawn from these measurements. It does seem however that the upturn is less and the absolute value lower than in the case of the strong anneal. Again, no indication of a pseudogap opening up was observed.

5 ARPES

5.1 Introduction

In the year 1886, Heinrich Hertz and his student Wilhelm Hallwachs discovered that a negative charged material could lose its charge under the influence of light. Although Alexandre Edmond Becquerel had already seen in 1839 that a conductive fluid could become a better conductor when exposed to light, Hertz's experiment was the first that clearly demonstrated the **photoelectric effect**. To explain why only negative charge and not positive charge could 'vanish' under the influence of light, two crucial ideas had to be put forward. The first came in 1899 when Joseph John Thomson introduced the electron, which he actually called corpuscles. The second was put forward 6 years later by Albert Einstein with the ingenious leap of mind of the quantization of light. This earned him the Nobel prize in 1923 and forms the basis for photoemission spectroscopy (PES) and its angular resolved (ARPES) version, the latter of which is used in this research and will be discussed in the next sections.

5.2 Theory [6]

By assuming light to be quantized in energy packets, or photons, Einstein wrote down an equation for the photoelectric effect (26) that fit experiments very well, but seemed to be completely at odds with the abundantly verified Maxwell equations which treats light as electromagnetic waves. Eventually the duality of light was acknowledged, but not without heavy debate. It took 10 years to confirm the linear relation between the energy of an emitted electron energy E_{kin}^{max} and the photon energy $h\nu$.

$$h\nu = E_{kin}^{max} - \Phi_0 \tag{26}$$

In equation (26) the constant Φ_0 is the energy required to excite an electron at the Fermi level into vacuum and is called the work function. Figure 22 gives a schematic view of the photoemission process, comparing the electronic energy distribution in a material with the measured electron energy spectrum. By analyzing not only the energy of the photoelectrons but also their angular distribution, i.e. momentum distribution, the band structure of a material can be probed directly. Figure 23(a) shows a schematic picture of an angle resolved photoemission (ARPES) setup.

The wave vector of the photoelectrons in vacuum for a certain emission angle is given by $\mathbf{K} = \mathbf{p}/\hbar$. The wave vector consists of a component perpendicular to the sample surface ($\mathbf{K}_\perp = \mathbf{K}_z$) and one parallel to it

---
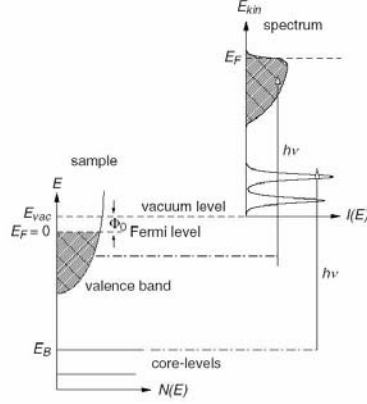
[6]This section is mainly based on [10]

Figure 22: Single particle picture of the photoelectric effect, where the work function Φ is the energy difference between the Fermi level energy E_F and the energy of an electron in vacuum E_{vac} [11].

$(\mathbf{K}_\| = \mathbf{K}_x + \mathbf{K}_y)$, which are given in terms of polar (θ) and azimuthal (Φ) angle by the following equations:

$$K_x = \frac{1}{\hbar}\sqrt{2mE_{kin}} \cdot \sin\theta \cdot \cos\Phi \tag{27}$$

$$K_y = \frac{1}{\hbar}\sqrt{2mE_{kin}} \cdot \sin\theta \cdot \sin\Phi \tag{28}$$

$$K_z = \frac{1}{\hbar}\sqrt{2mE_{kin}} \cdot \cos\theta \tag{29}$$

$$\tag{30}$$

where θ and Φ are the polar and azimuthal angle respectively as defined in figure 23(a). From the wave vector in vacuum, one would like to deduce the wave vector of the electron in the solid before it was excited by a photon. Since the system as a whole obeys the laws of conservation of energy and momentum, the following holds for an N-electron system:

$$E_f^N - E_i^N = E_{h\nu} \tag{31}$$
$$\mathbf{k}_f^N - \mathbf{k}_i^N = \mathbf{k}_{h\nu} \tag{32}$$

where i and f indicate the initial and final state of the system and $\mathbf{k}_{h\nu} = \frac{2\pi}{\lambda}$ is the momentum of the incoming photon. Since the momentum of a 21.2eV photon is $0.008\mathring{A}^{-1}$ which is 0.5% of the Bi-2212 Brillouin zone, its contribution to the total momentum can be disregarded. For an excitation to occur therefore, the lattice has to provide the momentum, which in the extended zone scheme is equal to a reciprocal lattice vector $\mathbf{G}$. Due to translational symmetry in the x-y plane across the surface of the crystal, the momentum parallel to the surface is conserved during a transition by an electron
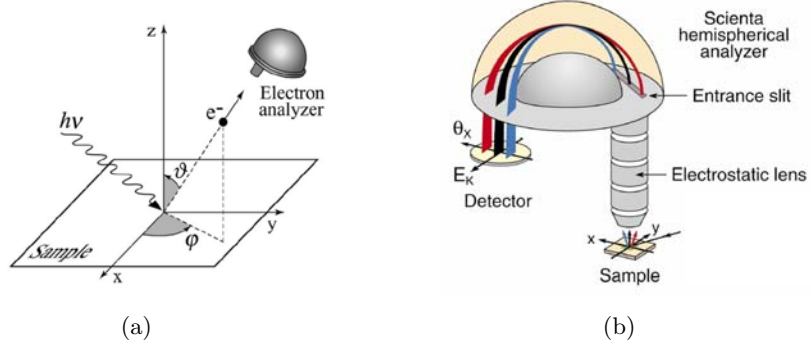
(a)   (b)

Figure 23: (a) Geometry of angle resolved photoemission spectroscopy, defining the polar (θ) and azimuthal (Φ) angle [10] and (b) a detailed view of the electron analyzer. A potential difference between the inner and outer hemisphere selects the energy of the electrons that fall onto the detector.

from solid to vacuum to within a reciprocal lattice vector parallel to the surface $\mathbf{G}_\parallel$. The momentum in the z-direction however is not conserved due to the abrupt change in potential across the surface. Since this component is also required to determine the electronic dispersion versus wave vector, either extra measurements or an a priori assumption have to be made, for instance band structure calculations. However, for nearly two dimensional system like BSCCO, the uncertainty in $\mathbf{k}_\perp$ is less important, since there is a negligible dispersion along the z-direction. The electronic dispersion is thus almost exclusively determined by $\mathbf{k}_\parallel$ and one can map the electronic dispersion simply by measuring the peak positions in energy as a function of $\mathbf{K}_\parallel$

$$\mathbf{k}_\parallel = \mathbf{K}_\parallel = \frac{1}{\hbar}\sqrt{2mE_{kin}} \cdot \sin\theta. \tag{33}$$

From this equation and neglecting the finite energy resolution, it follows that the momentum resolution of a setup with a certain finite acceptance angle $\Delta\theta$ is:

$$\Delta\mathbf{k}_\parallel \simeq \frac{1}{\hbar}\sqrt{2mE_{kin}} \cdot \cos\theta \cdot \Delta\theta. \tag{34}$$

The actual photoemission process is however much more complicated than the comprehensive picture sketched above, in which only uncorrelated electrons are concerned. In a strongly correlated electronic system like Bi-2212, many-body effects have to be taken into account.

The proper quantum mechanical way to describe the photoemission process is by considering a system with N electrons in a certain initial state Ψ_i^N that is excited by photons into a final state Ψ_f^N with a probability P_{fi}

that can be approximated by Fermi's golden rule:

$$P_{fi} = \frac{2\pi}{\hbar} | < \Psi_f^N | H_{int} | \Psi_i^N > \delta(E_f^N - E_i^N - h\nu) \qquad (35)$$

The delta function indicates that an electron will only be excited when the photon energy is exactly the difference in energy between the final and initial state. The excitation of an electron by a photon is described by the Hamiltonian H_{int}. This Hamiltonian is a perturbation of the unperturbed Hamiltonian, $H_0 = \frac{\mathbf{p}}{2m_e} + eV(r)$, given by the transformation $\mathbf{p} \to \mathbf{p} - \frac{e}{c}\mathbf{A}$ which gives the interaction of an electron with an electromagnetic field $\mathbf{A}$. The accompanying transformation in scalar potential can be omitted by choosing a proper gauge of the electromagnetic field (see Appendix A). The total Hamiltonian is the sum of the unperturbed and perturbed Hamiltonian, given by:

$$
\begin{aligned}
H &= \frac{1}{2m_e}(\mathbf{p} - \frac{e}{c}\mathbf{A})^2 + eV(r) & (36) \\
&= \frac{\mathbf{p}^2}{2m_e} + eV(r) + \frac{e}{2m_ec}(A \cdot p + p \cdot A) + \frac{e^2}{2m_ec}\mathbf{A}^2 & (37) \\
&= H_0 + H_{int} & (38)
\end{aligned}
$$

Since the quadratic term only becomes relevant when the electromagnetic field is very large, i.e. photon intensities are very high, this term can be neglected when using standard light sources in the laboratory. By using the commutation relation $[p, A] = -i\hbar\Delta \cdot A$, the perturbation Hamiltonian reduces to:

$$H_{int} = \frac{e}{2m_ec}(2\mathbf{A} \cdot \mathbf{p} - i\hbar\Delta \cdot \mathbf{A}) \qquad (39)$$

The last term in equation (39) can be set to zero using the dipole approximation. In this approximation the vector potential is constant over atomic scales, which holds in the ultraviolet region. At the surface of a crystal however, the electromagnetic field may have a strong spatial dependence, so this approximation may not be valid anymore. The one-step model of photoemission also takes these surface effects into account and describes the excitation of an electron in the bulk by a photon, transport to the surface and escape into vacuum as a single coherent process. However, since this model is quite complicated, photoemission data are usually analyzed within the three-step model, where these three processes (excitation, travel and escape) are treated as three separate processes. Although phenomenological, the three-step model has proven to be rather successful.

The probability of detecting a photoelectron within the three-step model becomes a product of the probability that a photon is absorbed by an electron, the scattering probability for the travelling electron and the probability that the electron escapes into the vacuum. The latter step depends on the

energy of the electron and the work function Φ, i.e. the electron can only escape when its kinetic energy is larger than or equal to the work function ($\frac{\hbar^2 \mathbf{k}_\perp^2}{2m_e} \geqslant |E_B| + \Phi$). An effective mean free path, proportional to the probability that an electron will reach the surface of a material without scattering, describes the second step. Since the main free path has a minimum of approximately 5 Å at 20-100 eV kinetic energies, a considerable fraction of the photoemission intensity will be representative of the topmost layer. Therefore fresh and flat surfaces have to be prepared in ultra high vacuum (UHV) with pressures lower than 10^{-10} mbar immediately prior to the experiment. Inelastic scattering of electrons during the transportation gives rise to a continuous background in the spectra, which can either be ignored, subtracted or even used to normalize the data. The first step, where an electron is excited by an electron, contains all the information about the intrinsic electronic structure of the material in question.

Returning thus to equation (35) and considering only bulk states, the dipole approximation can be made. A further simplification often used is by factorizing the final state into (N-1) electron terms and a photoelectron term. This **sudden approximation** physically means that the electron is assumed to be instantaneously removed from the system without interaction with the remaining material and the sudden removal of the electron results in a discontinuous effective potential of the system. Though the approximation is valid for electrons with a high kinetic energy, electrons with a low kinetic energy might need a longer time to escape the material than the system response time. In the latter case, the so called adiabatic limit, the sudden approximation is no longer valid and the final state wave function can no longer be factorized. For simplicity the sudden approximation will however be assumed to be valid, in which case the final state wave function can be written as:

$$\Phi_f^N = \mathcal{A}\Phi_f^{\mathbf{k}}\Psi_f^{N-1} \tag{40}$$

where $\mathcal{A}$ is the antisymmetric operator which ensures that the wave function satisfies Pauli's principle, Φ_f^k is the wave function of the photoelectron with momentum $\mathbf{k}$, and Ψ_f^{N-1} is the wave function of the final (N-1)-electron system.

If for simplicity the initial state is assumed to be a product of single electron wave functions, it can be written as:

$$\Phi_i^N = \mathcal{A}\Phi_i^{\mathbf{k}}\Psi_i^{N-1} \tag{41}$$

Inserting (40) and (41) into (35), one obtains for the matrix elements:

$$< \Phi_f^N|H_{int}|\Phi_i^N > = < \Phi_f^{\mathbf{k}}|H_{int}|\Phi_i^{\mathbf{k}} >< \Psi_f^{N-1}|\Psi_i^{N-1} > \tag{42}$$

where $< \Phi_f^{\mathbf{k}}|H_{int}|\Phi_i^{\mathbf{k}} > \equiv M_{f,i}^{\mathbf{k}}$ is the one-electron dipole matrix element. The final state wave function can be chosen to be an excited state with a wave function Ψ_m^{N-1}, so that the total probability of a transition is given by the sum over all possible exited states m. The total photoemission intensity as a function of energy E_{kin} and momentum k is then given by the sum over all possible initial and final states:

$$I(\mathbf{k}, E_{kin}) \propto \sum_{f,i} |M_{f,i}^{\mathbf{k}}| \sum_m |c_{m,i}|^2 \delta(E_{kin} + E_m^{N-1} - E_i^N - h\nu) \qquad (43)$$

where $|c_{m,i}|^2 = | < \Psi_f^{N-1}|\Psi_i^{N-1} > |^2$ is the probability that upon removal of an electron, the (N-1)-electron system will be left behind in the excited state m. Since in a strongly correlated system the removal of one electron will change the effective potential strongly, the initial state wave function will have overlap with many final state wave functions. Instead of a sharp delta peak at a single eigen-energy, several satellites are observed as well and a peak-dip-hump spectrum is obtained (figure 24).

In a strongly correlated system as discussed above, where many $|c_{m,i}|$ are
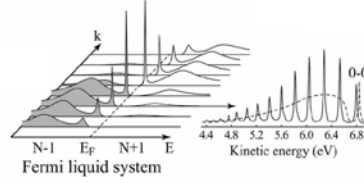

Figure 24: Peak-dip-hump spectrum as a consequence of overlap with many final state wave functions due to strong correlation in the system [10].

different from zero, the most powerful approach is by using Green's function formalism. Invoking the sudden approximation, this approach leads to an equation for the intensity measured from a 2D system using ARPES:

$$I(\mathbf{k}, \omega) = I_0(\mathbf{k}, \nu, \mathbf{A})f(\omega)A(\mathbf{k}, \omega) \qquad (44)$$

where $\mathbf{k} = \mathbf{k}_\parallel$, $f_\omega = (e^{\omega/k_b T} + 1)^{-1}$ is the Fermi-Dirac distribution[7] function which takes into account that only occupied states are probed by ARPES, A is the one particle spectral function and $I_0(\mathbf{k})$ is proportional to the squared one electron matrix element $|M_{f,i}^{\mathbf{k}}|$. The measured spectrum therefore does not only depend on the one particle spectral function, but also on the overlap of initial with final state wave functions, i.e. the matrix elements, plus a background from secondary electrons and the effects of finite resolution

---

[7]Angular frequency $\omega = 2\pi\nu$

of the system. The finite energy resolution can be estimated by fitting for instance a gold spectrum taken at an accurately known temperature to a Fermi Dirac distribution.

The matrix elements are an essential part of photoemission, since the geometry of a measurement can influence, via the matrix elements, what the measured spectrum will look like. If one considers a $d_{x^2-y^2}$ orbital, which has equivalent symmetry to the state the electrons in a high T_c superconductor close to the Fermi-energy are in, a mirror plane can be defined in which the state is either even or odd (see figure 25). For high symmetry
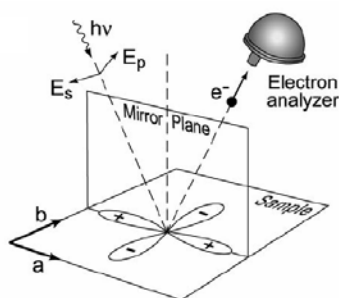

Figure 25: Schematic image of a $d_{x^2-y^2}$ orbital and its mirror plane. In this geometry, the d-wave has even symmetry with respect to the mirror plane. Rotating the orbital 45° either way gives an odd symmetry [10].

measurements, the photon beam and detector should be located in the mirror plane[8]. The wave function of the electron that will fall onto the detector (and thus $\Phi_f^{\mathbf{k}}$) will have to be even with respect to this plane, since odd parity wave functions are zero everywhere in the plane. For the same reason, $|M_{f,i}^{\mathbf{k}}|$ itself must be even with respect to the plane in order to have a non vanishing photoemission intensity. Therefore, $\Phi_i^{\mathbf{k}}$ and $H_{int} \propto \mathbf{A} \cdot \mathbf{p}$ have to be either both odd or both even for the matrix element to, as a whole be even:

$$< \Phi_f^{\mathbf{k}}|\mathbf{A} \cdot \mathbf{p}|\Phi_i^{\mathbf{k}} > \{ \begin{array}{llll} \Phi_i^{\mathbf{k}} & \text{even} & < +| + |+ > & \Rightarrow \quad \text{A even} \\ \Phi_i^{\mathbf{k}} & \text{odd} & < +| - |- > & \Rightarrow \quad \text{A odd} \end{array} \tag{45}$$

With an s-polarized[9] beam of light, only the odd initial state will be visible, whereas the even state will have zero intensity.

---

[8]If this is not the case and the photon beam and/or analyzer are in a different plane, the spectrum will be more difficult to interpret due to a lack of overall symmetry.

[9]The terminology s comes from the German word *s*enkrecht, which means perpendicular and therefore indicates that the direction of polarization is perpendicular to the mirror plane. p polarized light is polarized *p*arallel to the mirror plane.

The probability that an electron is excited by a photon depends on the interaction strength of the photon with a certain electronic state. If the initial and final state in equation (35) have significant overlap, the ionization cross-section will be high. Therefore, high energy photons will have a large ionization cross-section for electronic states with a high angular momentum. The photon energy dependence of photoemission is for instance important in resolving the bilayer splitting of the Bi-2212 main band (see section 5.4).

5.3 FAMoS

At the van der Waals-Zeeman Institute in Amsterdam where this master project took place, an angle resolved photoemission spectrometer by the name FAMoS (**F**OM **A**msterdam **Mo**mentum **S**pace microscope) is located. Figure 26 shows a picture of the FAMoS, indicating several vital parts of the machine. Aside from an intricate pump system to pump the sample
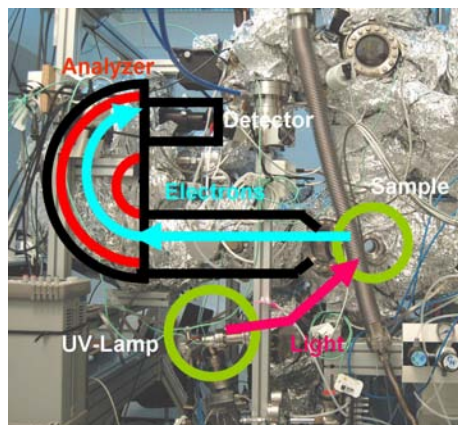

Figure 26: Picture of the FAMoS, indicating several vital parts (adapted from [39]).

space to ultra high vacuum and a cryostat that enables one to cool down to 5K, the machine basically consists of a light source, sample manipulator and analyzer.

The light source is a Gammadata VUV **helium lamp** in which helium gas is ionized by a spark plug. The ionized gas or plasma experiences a Lorentz force due to a static magnetic field and will start to rotate perpendicular to this field. If a dynamic electric field is applied perpendicular to the magnetic field, the electrons will accelerate in the direction opposite to the electric field. By tuning the electric and magnetic field such that the

angular frequency of both effects is equal[10], the electron cyclotron resonance is achieved and the plasma will be sustained. In the plasma, electrons in He atoms are continuously excited and will fall back under emission of a photon. The main transition lines are 21.2 eV (HeI α, 1s2p $\rightarrow$ 1s1s) which makes up 88% of the output intensity and 40.8 eV (HeII α[11], 2p $\rightarrow$ 1s) with 5% of the total intensity. The remaining intensity is made up of less probable transitions which will have to be filtered out before the light beam reaches the sample. To select only one excitation energy and filter out the unwanted energies, a toroidal monochromator is used.

The **monochromator** consists of a toroidal grating upon which the incident light is diffracted. Bragg's law

$$n\lambda = d\sin(\theta) \tag{46}$$

gives the relation between the wavelength of the diffracted light (λ), the diffraction angle (θ) and the spacing between the grooves of the grating (d). The angle between entrance and exit aperture of the monochromator is fixed at 140°, hence $\theta = 20°$. By changing the orientation of the grating, the effective groove size of the grating is adjusted to select either the 21.2 eV or 40.8 eV emission line of He, resulting in a well defined beam of light.

Since diffraction favors the polarization direction parallel to the grating, and the grating is oriented parallel to the mirror plane at the FAMoS, there is a p-polarization of the light beam (illustrated in figure 27). From equation
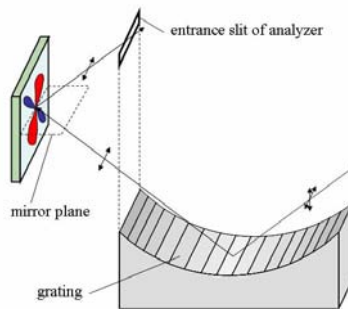

Figure 27: Light from the helium lamp is polarized parallel to the grating, resulting in a polarization parallel to the mirror-plane in which the projection of the incident beam and electron analyzer are located, i.e. p-polarization.

---

[10]The angular frequency due to a static magnetic field is $\omega = \frac{eB}{m}$, where $\omega = 2\pi f$. For a microwave frequency (f) of 10GHz, the magnetic field should be $\sim 0.36T$.

[11]the notation II indicates that the element is singly ionized, so in this case He$^+$, α is shorthand notation for the smallest transition possible, followed by β etcetera

(45) it can be seen that a p-polarized light source will only probe even states.

The **manipulator** of the FAMoS can change the polar and azimuthal orientation with respect to the analyzer slit. The FAMoS has a horizontal analyzer slit which means that one can scan radially through momentum space. This orientation is ideal to make Fermi surface maps which will be discussed throughout this thesis, but difficult for a measurement of the superconducting gap or pseudogap at the M-point.

The ejected photoelectrons are analyzed by a *Scienta* SES-2002 **hemispherical analyzer**. The analyzer consists of two concentric hemispheres with
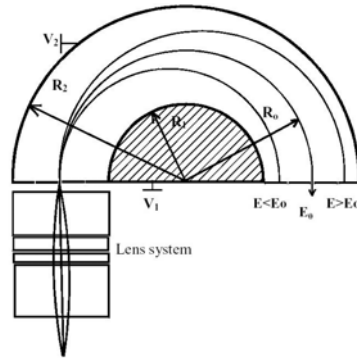

Figure 28: Schematic view of a typical electron analyzer [4].

radii R_1 and R_2 over which a potential difference can be applied[12] (see figure 28). By applying a voltage over the inner and outer hemisphere equal to

$$V_n(R_n) = \frac{E_0}{e}[\frac{2R_0}{R_n} - 1]$$ (47)

with n=1 or n=2, electrons with an energy equal to E_0 will follow a circular path with a constant radius R_0. Only electrons with an energy around the pass energy E_0 will thus fall on the detector. The energy resolution is then given by

$$\Delta E = E_0(\frac{w}{R_0} + \frac{\alpha^2}{4})$$ (48)

where w is the width of the entrance slit and α is the acceptance angle. Since the acceptance angle depends on the precise working of the lens system, and is therefore not well known, it is more useful to directly measure the energy resolution for a certain slit and pass energy. An experimental estimation of the energy resolution can be made by taking a spectrum of poly crystalline

---

[12]For the Scienta SES-2002, R_1=160mm and R_2=240mm, so R_0=(R_1+R_2)/2=200 mm.

gold with the settings that are used for the measurements on Bi-2212. The width of the transition at the Fermi energy is a result of broadening due to Fermi-Dirac statistics and the resolution of the machine, i.e.

$$\Delta E = \sqrt{\Delta T^2 + \Delta M^2}. \tag{49}$$

It is convention to define the width of the transition as the energy difference between 10% and 90% of the maximum intensity. Rewriting the Fermi-Dirac distribution function to become $\epsilon = kT \ln(\frac{1}{f} - 1)$, where ϵ is the energy relative to the Fermi energy, it can be seen that $\Delta T^2 = 2\ln(9)kT$. In this re-
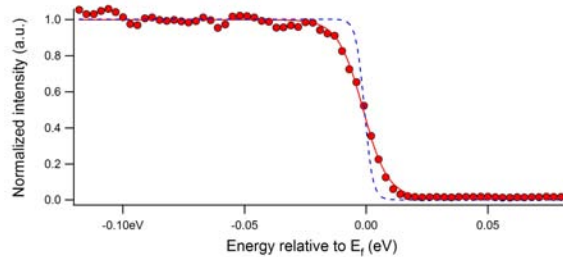

Figure 29: Cut at constant momentum of a photoemission measurement of gold taken at 25K with fit (solid line) and the Fermi-Dirac distribution function at the same temperature (dashed line).

search, the 0.5 mm curved slit with pass energy of 10 eV was chosen, giving an energy resolution of approximately 17 meV as determined by measuring the width of the Fermi edge of a gold sample at 25K (figure 29). A better resolution could be achieved by using a smaller slit or lower pass energy, but this in turn will lead to a lower electron intensity, i.e. less statistics for a measurement.

Before the electrons reach the entrance slit of the analyzer, five **cylindric lenses** retard the electrons to a selected pass energy and can either focus the electrons in an angularly or spatially resolved manner on the slit. By varying the voltages over the electrostatic lenses and thereby changing the retardation of the photoelectrons, a scan in energy can be made. The slit to the electron analyzer can be 0.2 to 4 mm in width and either straight or curved for the smallest slit widths. The latter option will correct the measured spectrum roughly for the spherical shape of the analyzer.

The **detector** is two dimensional position sensitive detector consisting of a two dimensional multichannel detector plate that multiplies the incoming electrons, a phosphor screen that produces a light flash when hit by electrons and a CCD camera which detects the light flashes. The position in both energy and momentum direction is thus conserved. The number of camera

channels that can record different momenta at the same time is maximally 127. Dividing the acceptance angle of 14° in 127 steps leads to a limiting resolution of approximately 0.1°, the true resolution however is $\sim 0.2°$ for the slit and pass energy used in this research[13].

5.3.1 LEED

Before a photoemission measurement is performed, it is worthwhile to do **L**ow **E**nergy **E**lectron **D**iffraction (hereafter LEED) first on the sample. Unlike in a LAUE experiment (section 3.3), in LEED the sample is not bombarded with polychromatic x-rays, but with monochromatic electrons. Since electrons have a much shorter main free path than x-rays, LEED is, like photoemission, very surface sensitive. Since LEED is performed with a single electron energy, a regular diffraction pattern is observed without the 'arrays' of dots as seen with LAUE. LEED can easily detect superstructure (doubling of spots) and the quality of the sample surface (sharp, bright spots). By scanning over the sample, the size of a good quality surface of the crystal can be determined. Most important, the orientation of the sample can be determined, saving a lot of time otherwise spent with finding the right orientation with photoemission.

---

[13]This resolution is more an indication than an absolute value, since it is quite difficult to devise a measurement which directly probes the momentum resolution. The theoretical resolution as given by equation (34) depends on the acceptance angle, which is in turn dependent on the lens system and therefore not precisely known

5.4   Fermi surface mapping of Bi-2212

As mentioned in section 2.3, the Fermi surface of a high T_c superconductor like Bi-2212 is nearly two dimensional and therefore ideal to study with angle resolved photoemission spectroscopy. The Fermi surface is given by the intensity maxima of a momentum distribution map (MDM) taken at the Fermi energy. The Fermi surface of Bi-2212 has several distinct features besides the main band due to its crystal structure, which will be discussed below. Figure 30 shows a schematic image of a unit cell of Bi-2212 together with its two dimensional Fermi surface. Since the BiO planes of different

(a)   (b)
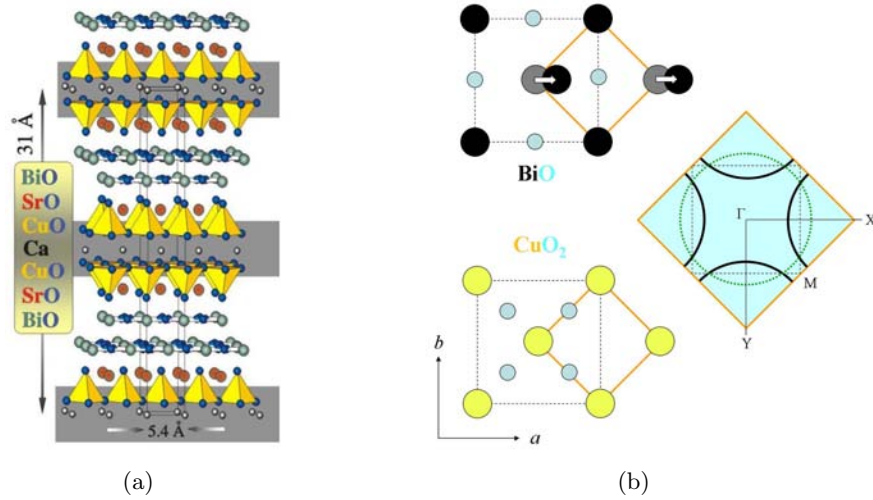
Figure 30: (a) Layered crystal structure of Bi-2212 with the size of a unit cell. (b) Schematic image of the Fermi surface of Bi-2212 with crystallographic notations (right) and CuO_2 plane (bottom). Both orthorhombic (dashed black) and tetragonal (solid orange) unit cell are shown, together with the shadow Fermi surface (dashed green) which is a consequence of the orthorhombic distortion of the central Bi atom (top) which is above the central Cu atom. The thick black arcs indicate the Bi-2212 bands at the Fermi level. The bilayer splitting is omitted for simplicity.

unit cells are only weakly bound by van der Waals interactions, these layers form the natural cleavage plane of Bi-2212. The lattice constant shown in the image is for the orthorhombic unit cell. However, the photoemission community often prefers to approximate the unit cell with a smaller tetragonal one, which gives $a \approx b \approx 3.8$Å. Strictly speaking this is an incorrect approximation since the central Bi atom in the BiO layer is shifted by $\sim 2\%$ of the orthorhombic unit cell length in the a-direction. The shift of the Bi atom first of all leads to an extinction in the LEED pattern in the ΓY direction (see figure 31). The full orientation of the sample can therefore be determined by a quick LEED scan. The distortion of the Bi atoms from the
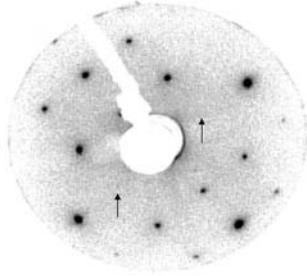
Figure 31: LEED pattern of Bi-2212 taken at 90 eV. Black arrows indicate missing spots due to the orthorhombic distortion of the Bi-atoms. For clarity the colors of the image are inverted.

tetragonal positions is furthermore felt by the nearby CuO_2 planes, affecting the electronic properties of the material.

5.4.1 Shadow Fermi surface

Recently it was shown that the so called **shadow band** can be attributed to the orthorhombic distortion [13]. The shadow band is a replica of the main band, centered around the Γ-point. By using polarized light in a high symmetry measurement it was observed that the shadow band has the same symmetry as the main band along the ΓX direction, but that it has a parity swap in the ΓY direction. If one considers an undistorted tetragonal system, only odd states with respect to both ΓX and ΓY are present which form the main band. Going to a real structure with an orthorhombic distortion, a shadow band appears, meaning that the shadow band wave function is the difference between the distorted and undistorted system. The overall distorted wave function $\Psi_D(x, y)$ can be written as

$$\Psi_D(x, y) = D(x)\Psi(x, y) \tag{50}$$

where $D(x)$ is the distortion in one direction in space and $\Psi(x, y)$ the undistorted wave function. Taylor-expanding the distortion to first order and neglecting higher orders since the orthorhombic distortion of the CuO planes in Bi-2212 is small, the total wave function becomes

$$\Psi_D(x, y) = \Psi(x, y) + xD'(0)\Psi(x, y). \tag{51}$$

The distortion responsible for the shadow Fermi surface is thus given by $xD'(x)\Psi(x, y)$, which is even in x since both x and $\Psi(x, y)$ are odd in x, explaining the parity swap observed. More detailed *ab initio* photoemission calculations support the comprehensive picture sketched above [32]. Since the shadow Fermi surface is a replica of the main band Fermi surface mirrored in the orthorhombic unit cell boundary, the $(\frac{\pi}{2}, \frac{\pi}{2})$-point can be easily

found by taking the midpoint between shadow band and main band. This will later on be used to correct for an unknown tilt component that was present during the measurements (see 5.4.5).

5.4.2   Bilayer splitting

Returning to the structure of Bi-2212, it can be seen that there are two CuO_2 planes separated only by a Ca layer. Each block of two CuO_2 planes is relatively isolated from other blocks by BiO and SrO layers. Overlap between the orbitals between the two CuO_2 planes in a block results in splitting of the band in a bonding and anti-bonding band. Detailed calculations already predicted this long before the bilayer splitting was first observed. The bilayer splitting should be maximal in the ΓM (antinodal) direction, while it vanishes in the ΓX and ΓY (nodal) directions, as a result of symmetry arguments. ARPES measurements indeed confirm this picture. However, as mentioned before, the sensitivity to probe a certain state with ARPES is photon energy dependent. Moreover, the symmetry of the bonding and anti-bonding bands within one bilayer block is even and odd respectively along the c-axis, which means their photoemission cross section is changed differently upon changing the incident photon energy. Whether the bonding or anti-bonding band or a mix of both is picked up in a measurement thus depends on the energy of the light used to excite electrons from the material. As will be seen in section 5.4.4, it is important to resolve both bands for a meaningful estimation of the doping concentration from ARPES measurements. An experimental survey of the relative intensities of the bonding and anti-bonding band for different excitation energies is summarized in figure 32. It can be seen that at a photon energy of 21.2 eV which is used in this
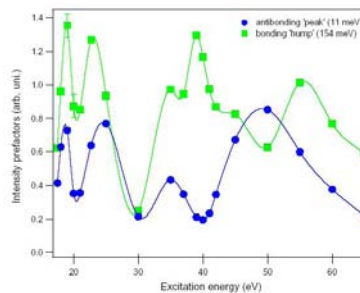

Figure 32: Excitation energy dependence of the matrix elements of the bonding and anti-bonding band as fitted from cuts in the MX direction at the M-point [14].

research, the bonding band is the most pronounced component.

Besides the photon energy dependence, polarization and temperature can also influence the relative intensities of bonding and anti-bonding band. As mentioned the bonding and anti-bonding band have opposite symmetry in the c-direction, hence they will react differently to a different polarization. Since the anti-bonding band is just below the Fermi level, it is much more influenced by Fermi-Dirac temperature broadening. Therefore the room temperature intensity maxima are mainly determined by the bonding band, while low temperature photoemission can have a considerable contribution from the anti-bonding band.

5.4.3 Diffraction replicas

Non lead-doped Bi-2212 has a periodic superstructure of approximately 5 lattice spacings (tetragonal spacings, 5.4Å) in the b-direction of the crystal. Scattering off this superstructure by photoemission electrons leads to diffraction replica's of the main band along the ΓY-direction. As can be seen in figure 33, the presence of diffraction replicas is a major problem in analyzing the photoemission data. Especially around the M-point, where the bilayer splitting is the most pronounced, it becomes nearly impossible to tell main band from diffraction replica and shadow band. Substituting
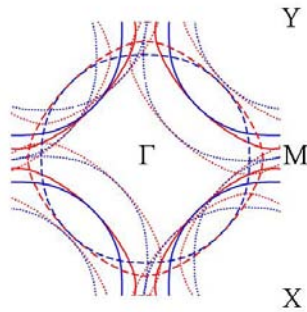

Figure 33: Schematic image of the Fermi surface of non lead-doped Bi-2212. The solid lines are the main band, red and blue are anti-bonding and bonding band respectively. Dashed are the shadow Fermi surfaces and dotted the diffraction replicas. Diffraction replicas of the shadow Fermi surface are omitted, for simplicity.

about 20% of Pb atoms for Bi suppresses the superstructure leading to a spectrum without diffraction replicas.

5.4.4 Hole doping concentration

The Fermi surface of a high-T_c superconductor contains a lot of information about the material. If the exact locus of the Fermi surface is known, for

instance from a normal state measurement, analysis of the superconducting gap as function of position in momentum space can be performed. From this in turn the type of superconductivity can be determined, for instance d-wave superconductivity for Bi-2212.

The Fermi surface moreover contains information on both the carrier type and concentration. Whereas the Brillouin zone is defined by the crystal lattice which is formed by the atoms, i.e. by the periodic lattice potential, the Fermi surface is determined by the electronic configuration of those atoms. Considering only the two dimensional CuO_2 planes, the electronic states close to the Fermi level are the Cu $d_{x^2-y^2}$ and the O p_x and p_y orbitals. In the undoped antiferromagnetic mother compound of Bi-2212 the $d_{x^2-y^2}$ orbital is occupied by one localized electron, while the p-orbitals are all filled. Therefore the first Brillouin zone would be exactly half filled with occupied states. On the other hand, if the system would have exactly two electrons in the $d_{x^2-y^2}$ orbital, the first Brillouin zone would be completely filled. If S_{FS} is the area of the Fermi surface and S_{BZ} is the area of the first Brillouin zone, then for the half filled system $\frac{S_{FS}}{S_{BZ}} = \frac{1}{2}$, which corresponds to a doping of x=0. For the filled system $\frac{S_{FS}}{S_{BZ}} = 0$, corresponding to a doping of x=-1 (positive x indicates holes, while in this scenario electrons are doped). Combining these relations, the following relation for the doping is obtained:

$$1 + x = \frac{2S_{FS}}{S_{BZ}}. \tag{52}$$

Upon introducing holes into the half filled system, the area in k-space of states filled by electrons decreases, i.e. the Fermi surface closes in on the Γ-point. The shape of the Fermi surface is subsequently determined by the type of state close to the Fermi level, in the case of Bi-2212 leading to Brillouin zone crossings around the M-points, where the lobes of the orbitals point at.

The tetragonal unit cell of Bi-2212 has a lattice constant of 3.8 Å. The square first Brillouin zone has therefore a reciprocal lattice constant of $\sim$ 2×0.82 Å^{-1} and corresponding area of (2.69 Å^{-1})^2. If one can measure the exact area of the Fermi surface, for which reason it is important to resolve the anti-bonding band, the doping concentration can be estimated and cross referenced to other methods like superconducting gap analysis, transition temperature and presence of a pseudogap phase in resistivity measurements.

5.4.5   Tilt

The FAMoS has two controllable angular degrees of freedom, polar and azimuthal angle. However, there is a third degree of freedom which affects the spectrum, but cannot be controlled, namely tilt (see figure 34). The
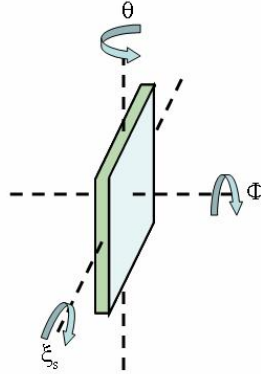
Figure 34: Three degrees of freedom of a sample: polar, azimuth and tilt. Since the effect of the sample tilt depends on the azimuth an extra term, α, appears in the equations for k_x and k_y which accounts for this azimuthal offset.

tilt can be divided into a mechanical contribution, i.e. misalignment of the manipulator with respect to the electron analyzer, and a sample tilt. A sample tilt can arise when the sample is not completely flat, when it is not glued perfectly parallel to the sample holder, or when the sample holder is placed into the manipulator pocket under a slight angle. The projection of k-space that falls onto the slit is determined by both the polar and azimuthal angles, as well as both types of tilt components. The momentum vector components k_x and k_y (equation 27) that fall onto the slit, can thus be derived using standard trigonometry:

$$
\begin{aligned}
k_x &= \frac{1}{\hbar}\sqrt{2mE_{kin}}[\sin(\theta + \xi_s \cdot \sin(\phi + \alpha))\cos\phi - \\
&\quad \sin\phi\cos(\theta + \xi_s \cdot \sin(\phi + \alpha))\sin(\xi_m + \xi_s \cdot \cos(\phi + \alpha))] \tag{53}
\end{aligned}
$$

$$
\begin{aligned}
k_y &= \frac{1}{\hbar}\sqrt{2mE_{kin}}[\sin(\theta + \xi_s \cdot \sin(\phi + \alpha))\sin\phi + \\
&\quad \cos\phi\sin(\theta + \xi_s \cdot \sin(\phi + \alpha))\sin(\xi_m + \xi_s \cdot \cos(\phi + \alpha))] \tag{54}
\end{aligned}
$$

where α is the azimuthal offset of the sample tilt. The effect of both a sample and mechanical tilt on the projection of k-space onto the slit are shown in figure 35. To correct the measurements for angular distortions a program has been written in the framework of this masters project, of which the details can be found in appendix C.

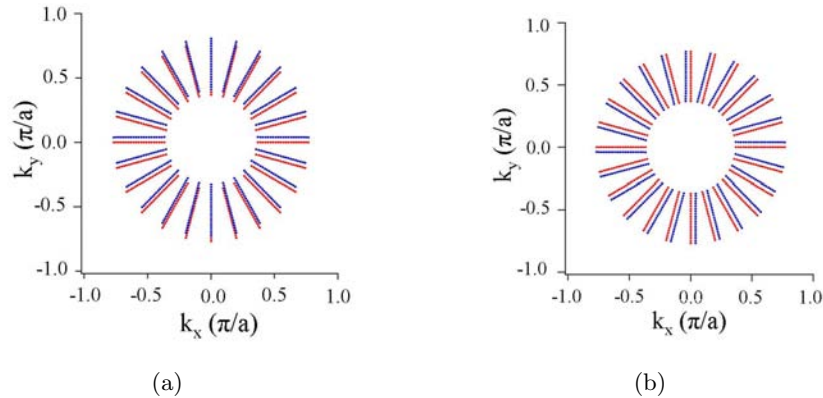(a)   (b)

Figure 35: Projection of k-space onto the slit for (a) a sample tilt of 2° and (b) a mechanical tilt of 1° (shown in blue) compared to a perfect alignment, i.e. no tilt (shown in red).

5.5   Photoemission measurements on Bi-2212

Photoemission measurements were performed on several samples having had different post anneals. The samples were glued with silver epoxy to the sample holder for good thermal contact and pre-cleaved before placing a loop of tesa tape on it. After insertion in the FAMoS, cleavage was done at room temperature at a pressure of less than 5×10^{-11} mbar. All measurements discussed in the following were performed on flat and shiny surfaces as determined by eye after cleavage. Subsequently, LEED was performed to examine the crystallinity and quality of the surface layer on which the photoemission measurement was to be carried out. Only samples with a region of sharp, single spots over an energy range of several tens of eV were subsequently measured. Samples with a very small region of good spots, or those with double or vague spots, were not measured. After determining the orientation of the sample, aided by the extinctions in the ΓY-direction, the sample was slowly cooled to approximately 25 K.

5.5.1   Fermi surface mapping

The FAMoS has a horizontal slit, which means that image on the detector maps k-space radially away from the Γ point (see figure 35). Increasing the polar angle will move the image away from the Γ-point, while a rotation of the azimuthal angle will rotate the image around the Γ-point. For the HeI-line of 21.2 eV which was used for all measurements, the M-point is located at a polar angle of approximately 21 degrees. Since the slit has a width of 14 degrees, a fixed polar angle of 16 degrees was chosen in order to have both the M-point and X- and Y-points, which are at 12 degrees polar, on the slit. To make a map of the Fermi surface, only the azimuthal angle

has to be changed from one scan to the next. In order to correct for angular distortions, the azimuthal range was at least 180 degrees, so three M-points and the X- and Y-points were measured.

Previous research [39] on Bi-2212 has shown that samples are subjected to aging during measurement. After more than about 6 hours, the surface layer of a sample has changed too much for the measurements to be representative, and the sample has to be taken out and re-cleaved. For high statistics on a single measurement, the time over which a scan is averaged should be as large as possible. Moreover, the energy-range at which scans are made should include at least several tens of meV above the Fermi level and even more below. For a high energy resolution needed to do analysis on the superconducting gap, the stepsize in energy should be small. Furthermore, in order to have a high angular resolution of the Fermi map, the azimuthal stepsize should be as small as possible. An optimum combination of these factors thus has to be found since there is only 6 hours of measuring time per cleave. The Fermi surface maps discussed in the following have an azimuthal step size of $3°$ or $4°$ with a range of over 190 degrees. Energy steps of 3 meV were used for a total range of 200 meV. The time constant was then chosen such that the total map would take just under six hours, which in practice means about 0.6 seconds per energy step.

For a successful map of the Fermi surface, a region on the sample has to be found which has a high photoelectron count-rate for more than 180 degrees of azimuthal rotation. In practise this is not always the case. Therefore not only azimuth, but also the height and xy-position of the sample have to be altered between sets of measurements. These separate blocks of the total map can afterwards be combined. However, a change of other parameters than azimuth might lead to a slight change in polar or tilt, if the sample is for instance not completely flat. Corrections have to be made for these slight distortions.

Due to the curved path of the photoelectrons before reaching the detector, the recorded image is also slightly curved. All measurements were therefore first corrected for this effect using a scan of an essentially amorphous gold film, which has a k-independent Fermi level[14]. Normalization to the detector sensitivity along the energy axis of the detector is already accounted for by measuring in swept mode as opposed to fixed mode. In swept mode, the electrostatic lenses sweep through the energy that will fall onto the center of the detector. Each row of energy channels will thus have had all measured

---

[14]To each column of angular channels a Fermi Dirac function is fitted, giving the Fermi energy for all detector angles. This in turn is used to correct the images from single crystalline samples.

energies on each channel, which is summed by the measurement software. To compare scans with a different azimuthal angle, normalization to high energy photoelectrons is done. Since the monochromator is not perfect, a small part of high energy photons (40.8 eV (HeII) photons for instance) also reaches the sample, leading to a background of high energy photoelectrons. The photoelectrons that are emitted by these high energy photons and are subsequently detected are therefore electrons with a relatively high binding energy. These can to a good approximation be assumed to be independent of k and thus of angle[15].

After combining all measurements of one cleave to form a Fermi surface map and normalizing it, angular corrections have to be done. First a total of 20
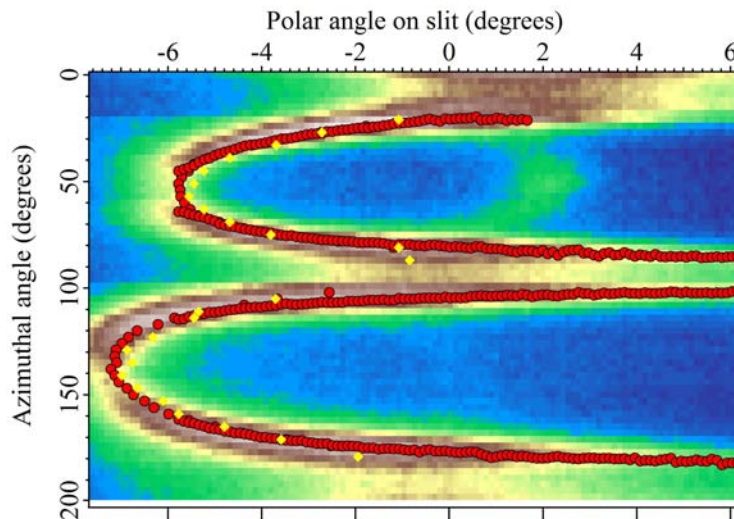

Figure 36: Comparison of fits to the peak-intensity (red) and the leading edge (yellow) for the AG0606 sample. On the horizontal axis is the polar angle on the slit. The vertical axis shows the azimuthal angle.

meV around the Fermi level is integrated for better statistics (-10 meV to 10 meV). Since 20 meV is approximately the energy resolution of the setup, the loss of information due to integration is kept to a minimum. The resulting MDM (Momentum Distribution Map) can then be fitted with Lorentzians to determine the peak-intensity positions. Generally, the leading edge closest to the Fermi energy gives the location of k_f, where the leading edge is usually taken to be the midpoint between 90% and 10% of the maximum of an MDC. Since the leading edge is however more difficult to determine automatically than the peak position of an EDM at the Fermi level, the latter procedure has been adopted to find k_f. The difference between the

---

[15]Care should be taken not to excite core levels with HeII light.

two methods depends on the steepness of the bands. For steep bands, the leading edge and peak are located nearly on the same location. Since the bands are steeper at the nodal points [36], the difference is expected to be smaller there than at the anti-nodal points. However with the geometry of the FAMoS (horizontal slit) it is difficult to determine the leading edge at the M point precisely, and the error in k_f due to peak fitting will be approximately similar over the entire Fermi surface arc. Figure 36 shows an image of a typical MDM with fitted peak-intensities plotted on top. Leading edges of several slices are determined by fitting EDC's with a convolution of a Lorentzian and a Fermi Dirac distribution to determine peak position and height. A manual check afterwards confirmed that the fitting went properly. The leading edges are also plotted in figure 36. The error in determination of k_f by considering peak-intensities instead of leading edges is acceptable. Since the map is made in the superconducting state, a superconducting gap opens up and the leading edge or peak intensity do not necessary give the location of k_f. Ideally, a room temperature map should be made, from which k_f is determined. A second measurement with the same settings can then be made in the superconducting state which can be analyzed using the room temperature determined k_f's. The low temperature measurements will however have to be performed after cleaving the sample again because of aging. Since it is not completely certain that measurements on different cleaves can be compared quantitatively due to uncontrollable angular distortions, it was decided here to analyze only low temperature measurements. The error due to the opening of a gap should therefore be taken into account.

Once the location of k_f is known, corrections for the angular distortions can be made by fitting the experimental Fermi surface profiles to tight binding calculations, given by the equation

$$E = dE - 2t(\cos k_x + \cos k_y) - 4t' \cos k_x \cos k_y - \qquad (55)$$

$$2t"(\cos 2k_x + \cos 2k_y) \mp t_\perp \frac{(\cos k_x - \cos k_y)^2}{4}$$

where the plus (minus) sign corresponds to the anti-bonding (bonding) band. The fitting procedure can be made more robust by including a second energy level below the Fermi level, for instance 80 meV below E_f. The energy offset dE will be more reliable in that case and consequently the hopping parameter t, t' and $t"$ as well. The remaining parameter, $t_\perp$, gives the strength of the bilayer splitting. Figure 37(a) shows schematically how $t_\perp$ is defined. Since at the excitation energy of 21.2 eV mainly the bonding band is observed and no bilayer splitting is resolved directly in the experimental data, it is difficult to determine $t_\perp$. Therefore, data taken at the SLS synchrotron on a samples with a similar doping concentration which did show bilayer splitting (due to use of a different measurement geometry and photon energy), were used to determine $t_\perp$ (figure 37(b)). Moreover, according

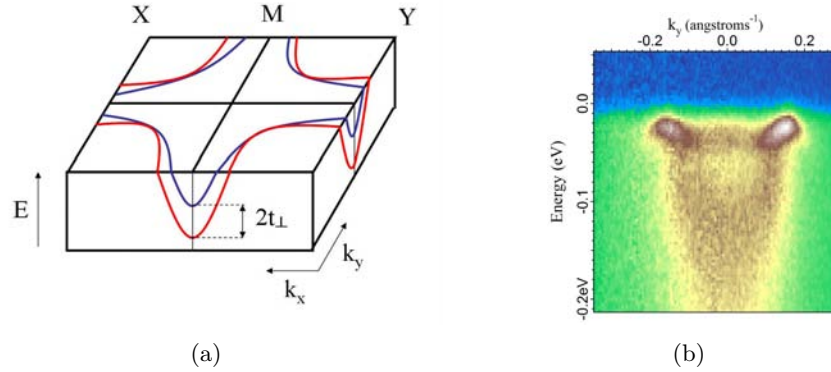(a)   (b)

Figure 37: (a) Schematic image of the first Brillouin zone with the anti-bonding (red) and bonding (blue) bands. $t_\perp$ is given by half the difference between the bands at the M-point. (b) XMY-cut taken at the SLS synchrotron showing the bilayer splitting. $t_\perp$ is approximately 55 meV. In red and blue are as a guide to the eye the bonding and anti-bonding band respectively.

to literature [18] the splitting is doping independent, so $t_\perp$ is approximately constant for all data sets considered here. Once the bonding band is fitted and the bilayer splitting is estimated from the synchrotron-based measurement, the doping concentration can be calculated using equation (52)

To summarize the above, the following steps are gone through from cleaving the sample to an estimate of the doping concentration:

1. Fermi surface measurement

2. Normalization to gold

3. Location of k_f by fitting peak-intensities

4. Correction for angular distortions

5. Fitting to tight binding calculations

The hole concentration per Cu atom is then given by the average of the doping concentrations from the bonding and anti-bonding band. Figure 38 shows a typical Fermi surface map and a map at 80 meV binding energy taken at the FAMoS after normalization and correction for angular distortions. Also shown are the tight binding fits of the bonding (red) and anti-bonding (blue) band. At the Fermi level, the intensity comes mainly from the region around the nodes[16], whereas at 80 meV binding energy, the situation is reversed and the anti-nodes give the highest intensity. The former

---

[16]the intensity exactly at the node is less since the main band has odd symmetry and the incoming light is p-polarized (see section 5.3)
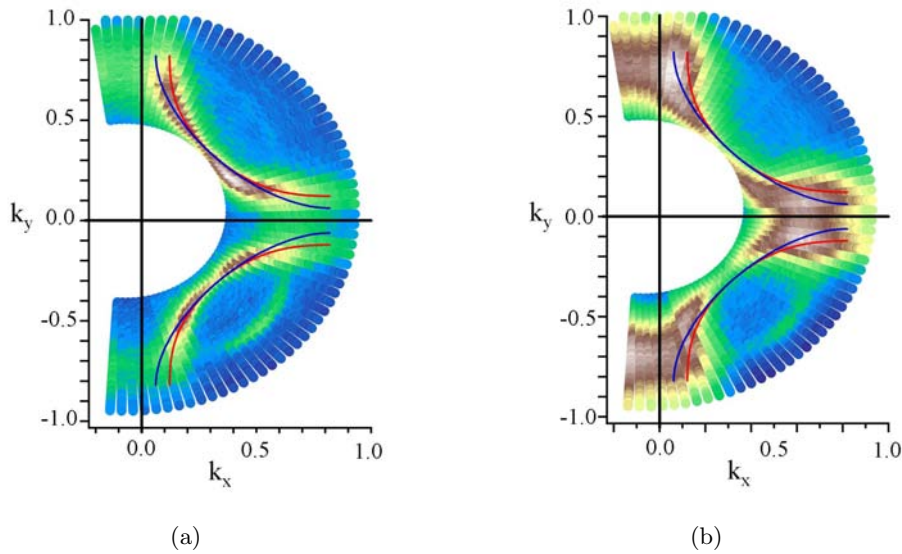
Figure 38: (a) Fermi surface map and (b) map at 80 meV binding energy of AG0606. The red and blue curves are tight binding fits of the bonding and anti-bonding band respectively. Both maps are measured in the anti-clockwise azimuthal direction.

can be explained by a vanishing superconducting gap at the node (d-wave character), while the latter is due to the underlying band structure. The shadow band is mainly visible in the Y-quadrant as expected for the polarization and geometry of the FAMoS, which attests also to the non-twinned nature of the samples used. Non-uniform intensity of the main band over the entire map can be attributed to several factors. Sample inhomogeneities might cause differences since the sample is rotated over more than 180 degrees during the measurement. Loss of intensity due to aging might also contribute, as well as slight fluctuations in the spectrum of the lamp. Also broadening of the peaks in the ΓY-direction due to weak diffraction replica's resulting from residual, small superstructure might occur.

The tight binding fitting parameters correspond to literature values [33] which is a strong indication that the procedure adopted to distill a doping concentration works properly. Figure 39 shows one fourth of the Fermi surface barrel (the ΓY-quadrant) shown in figure 38 with tight binding fits of the bonding (red) and anti-bonding (blue) bands. The intensity of the individual scans that make up the Fermi map is manually adjusted, so that the intensity differences at peak positions are smaller. The area between different scans is filled with interpolated values, i.e. data is generated to visualize the bands more clearly. As can be seen in the image, the shape and location of the measured Fermi surface are fitted well by the tight binding

calculations. A hole doping concentration of approximately 0.22 is found
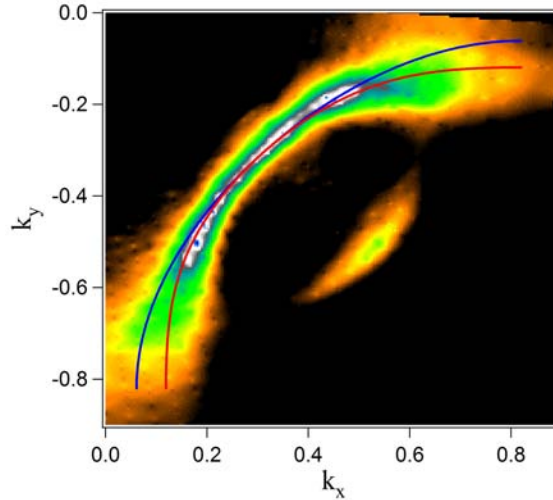

Figure 39: ΓY-quadrant of the AG0606 sample, where peak intensities are scaled to each other and the space between the individual scans is filled with interpolated values. The Fermi arc is fitted well by tight binding calculations.

with an error of ±0.04 holes per Cu-atom for the sample shown in figure 38. The error in the doping concentration depends mainly on the corrections to angular distortions. Tight binding fits have been made to several different angular corrections from which the optimum fit is extracted with its error. The error is quite large and could be reduced by for instance taking smaller steps in azimuth and adding further measurements in the second Brillouin zone. Estimated doping concentrations with their errors for samples from different anneals with different superconducting transition temperatures are plotted in figure 40. The commonly used empirical relation of T_c versus hole doping is plotted as a dashed line. Since the errors in the doping concentration are considerable, one would be brave to claim these data give evidence of success in terms of reaching the underdoped state of (Pb,Bi)-2212. This could be argued to be all the more valid since the sample which had undergone an oxygen anneal (O), and is thus definitely not underdoped, seems to be leaning towards the underdoped side of the phase diagram. The corrected Fermi surface maps from which the doping concentration is calculated are also shown in figure 40. All original, half Brillouin zone maps have been rotated around the Γ-point in order to obtain a Fermi surface map of the complete first Brillouin zone. The effect of symmetrization is clearly visible. At k-values where no direct measurements were performed, interpolated values are plotted. Where necessary, peak intensities per measured azimuthal
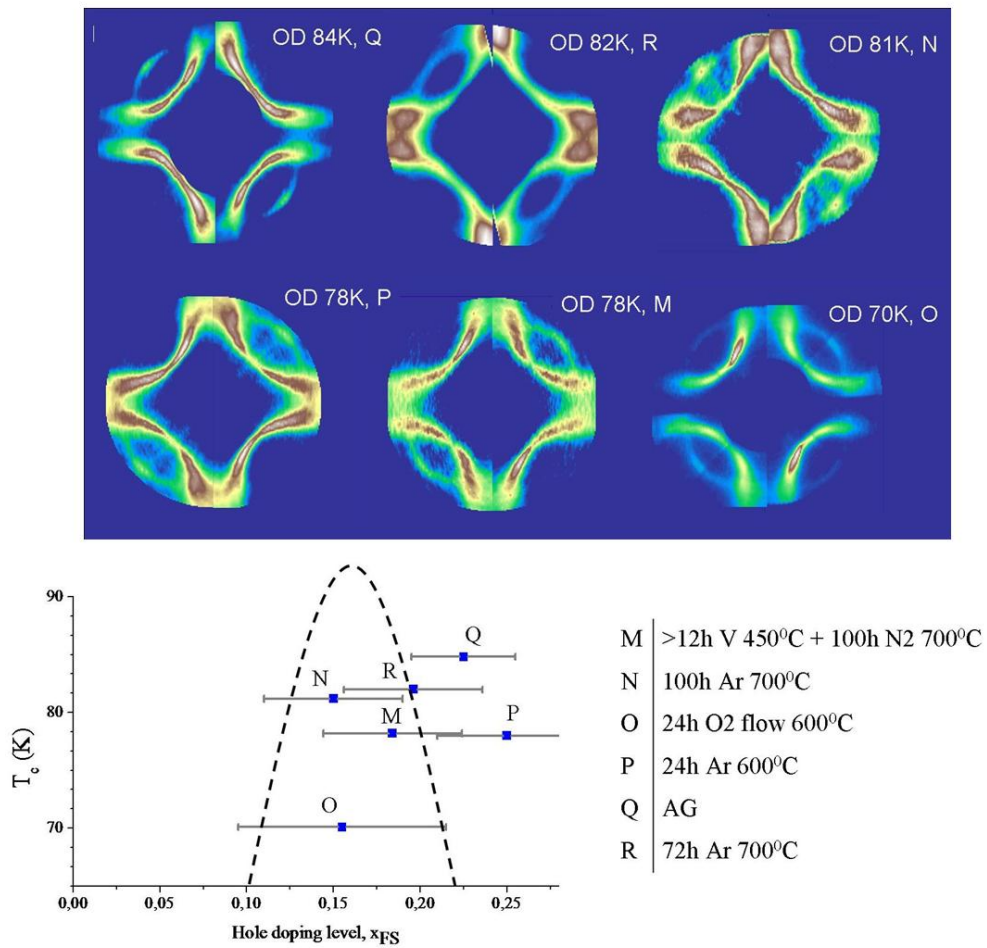
Figure 40: Doping concentration calculated from tight binding fits of Fermi surface maps (top) versus T_c after correcting for angular distortions. The dotted line indicates the commonly used empirical relation between T_c and the doping level [26]. Sample M has been measured by E. Slooten, R and P by S. de Jong.

angle have been corrected slightly so the main band has a more or less equal intensity over the entire Fermi surface arc. The image on the front cover of the thesis shows multiple first Brillouin zones put together to form full Fermi surface barrels. This is a nice demonstration of the correspondence between experiment and theory and a confirmation of the validity of the method of correcting angular distortions.

5.5.2   Superconducting gap analysis

A commonly used empirical measure of the superconducting gap in photoemission data is given by the difference between the leading edge and the Fermi level for a k_f energy distribution curve. For all fitted peak-positions, the leading edge has been determined by fitting a Lorentzian and a Fermi Dirac function to the EDC's described previously. Plotting the superconducting gap versus the Fermi surface angle (see figure 41(a)), the gap size can be examined as a function position of the band in k-space. Figure 41(b) shows the Fermi surface dependence of the gap for the same sample for which the Fermi surface map is shown in figure 35. The large number of points is an artifact of the method which is adopted to find k_f positions. Whereas per measurement at a single azimuthal value, there will be only one real k_f, it might be possible that several 'k_f's' per measurement are used for analysis on the superconducting gap. Especially at the M-points, where peaks are fitted perpendicular to the slit (fits to azimuthal momentum distribution curves) the point density is therefore artificially large. The data can be fitted with a theoretical d-wave function [12]:

$$\Delta(\phi) = \Delta_0 |B\cos(2\phi) - (B-1)\cos(6\phi)| \qquad (56)$$

in which Δ is the superconducting gap size, Δ_0 the maximum gap and B a doping dependent fitting parameter. For B=1, a pure d-wave is obtained. For underdoped samples however, B has been reported [34], [35] to decreases, and the relatively sharp 'V' form of the gap function around the nodal line changes to a less sharp 'U'-like form. For the data shown in figure 41, $\Delta_0 \approx 20$ meV and B=0.86, where B=1 is also within the experimental error (shown in the graph with a black dashed line). Three other measurements which are not shown gave the same parameters, which are all in correspondence with literature. A smaller superconducting gap for two samples can be attributed to a higher temperature during the measurement (the superconducting gap is a monotonically decreasing function of increasing temperature). The superconducting gap increases upon decreasing the doping concentration. However, since no superconducting gap larger than ∼20 meV is found on any of the samples, is can be assumed than no underdoped samples were present. To make sure the method adopted of determining k_f by fitting the peak-intensity was acceptable, the superconducting gap is also determined for the blue points in figure 36, i.e. from the
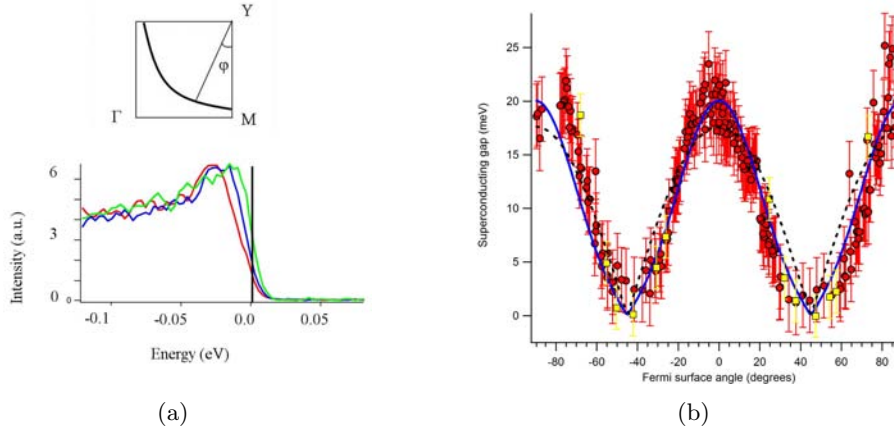
Figure 41: (a) (bottom) Shift of the leading edge, going from the node to the anti-node, due to opening of the superconducting gap. (top) The definition of the Fermi surface angle (ϕ) is shown, where $\phi=0$ corresponds to YM. (b) Superconducting gap versus Fermi surface angle for AG0606. In red are the gaps at the fitted peak-intensities, which are comparable to the gaps at the highest leading edge (yellow). A fit to equation (56) with $\Delta_0=20$ meV and B=0.86 is shown in blue. Dashed in black is a pure d-wave gap function (B=1).

k_f locations following from a 'minimum leading edge' analysis. The latter were found by finding the highest leading edge per scan. The gaps thus determined are plotted in yellow in figure 41(b). Both methods of determining k_f give an almost identical superconducting gap size, which confirms that the adopted method is valid.

6   Conclusions

Resistivity and photoemission measurements have been performed on (Pb,Bi)-2212 samples annealed with several different procedures. For none of the samples a downturn in in-plane resistivity is observed which would indicate the opening of a pseudogap gap. Instead an upturn just above the superconducting transition temperature is seen in many samples. This is likely to be a result of disorder in the samples due to aggressive annealing, aimed at achieving underdoping. Hole doping concentrations determined by tight binding fits to Fermi surface maps seem to confirm the absence of underdoped samples. No superconducting gap is found to be larger than ~ 20 meV, while for underdoped samples this should be larger [34], [35]. Combining all results, it can therefore with a relative high certainty be concluded that the methods so far used to change the doping concentration have not led yet to an underdoping of the samples. Surprisingly, there are many articles claiming to obtain underdoped samples with similar annealing treatments [19], [20]. In most cases, these samples are non Pb-doped. Therefore it might be possible that the lead changes the crystal structure in such a way that it is much more difficult to change the oxygen content in the CuO_2-planes. To investigate such a scenario, Pb-doped and non Pb-doped samples have been annealed with the same aggressive vacuum anneal. However, during the annealing process, the samples got mixed up and afterwards it was difficult to separate them again. LAUE images seemed to indicate that the non Pb-doped samples lost their crystallinity almost completely, while the Pb-doped ones still showed clear diffraction spots. This could confirm the fact that a change of structure becomes much more difficult with Pb-doping. A more thorough investigation by resistivity measurements was limited due to technical reasons. Since Pb-doping is essential for proper analysis of photoemission measurements, underdoping might be achieved by for instance Y substitution of Sr.

In order to do reliable resistivity measurements on Bi-2212, a method of making electrical contacts has been devised which has a relative high success-rate, yielding acceptable contact resistances and long lifetime. Resistance measurement tests using the same contact 'recipe' on the giant magneto resistance material $LaSr_2Mn_2O_7$, which has also a bilayer perovskite crystal structure, were promising. Due to possible malfunctioning connections somewhere inside the measuring system (MagLab) regular tests with known resistances are advisable. This excludes uncertainty about the measurement due to hard- or software problems so measurements can be regarded as purely due to the sample. Also the effect of one or more bad contacts could be simulated with known and/or variable resistances in order to have a better idea of the measuring system.

7   Nederlandse Samenvatting

Elektriciteit is een essentieel onderdeel van de hedendaagse samenleving. Hoog verbruik van een slinkende voorraad fossiele brandstoffen bedreigt echter de energie- en dus electriciteitsvoorziening van de wereld. Een aanzienlijk deel van de oorspronkelijke energie gaat verloren aan transport alleen, bijvoorbeeld doordat elektriciteitsdraden opwarmen. Dit laatste komt doordat elektronen botsen op atomen en zo hun energie afgeven, nog voordat het uiteindelijke doel is bereikt. Met andere woorden, de elektriciteitsdraad heeft een bepaalde weerstand.

In sommige materialen, bijvoorbeeld kwik, verdwijnt de weerstand echter plotseling als het onder een bepaalde temperatuur gekoeld wordt. Dit betekent dat een stroom onbeperkt door een zogenaamde supergeleider kan stromen: de geleidende elektronen worden op geen enkele wijze verstoord. Naast een enorme mogelijke energiebesparing heeft een supergeleider nog andere interessante eigenschappen. Een extern magneetveld zal door kringstromen perfect kunnen worden tegengewerkt, waardoor er binnenin de supergeleider geen veld is. Ook kunnen zeer hoge magneetvelden worden opgewekt met supergeleidende spoelen. De spoelen zullen in tegenstelling tot normale spoelen niet doorbranden als er een hoge stroom doorheen wordt gestuurd (zolang de supergeleider maar supergeleidend blijft!).

In een supergeleider vormen de elektronen zogenaamde Cooper-paren, ondanks dat ze elkaar normaal afstoten vanwege hun negatieve lading. De 'lijm' die de elektronen bij elkaar houdt wordt door het atoomrooster van de supergeleider geleverd. Het gevolg van paarvorming is dat de botsingen die voor weerstand zorgen niet meer optreden. De paarvormings-interactie wordt echter tegengewerkt door thermische activiteit van de elektronen in de supergeleider. Hierdoor treedt supergeleiding alleen bij extreem lage temperaturen in, voor een grote groep materialen pas onder de -250°C. Om een materiaal op een dergelijke lage temperatuur te krijgen en houden, kost meer energie dan het ontbreken van weerstand oplevert. Nu is er een aparte groep supergeleiders die boven -197°C al supergeleidend worden. Aangezien koeling met rijkelijk aanwezig en goedkoop vloeibaar stikstof dan al genoeg is, kan met deze materialen daarwerkelijk energiewinst worden geboekt. Misschien is er zelfs wel een materiaal met een nog hogere overgangstemperatuur (T_c) naar de supergeleidende toestand.

De sleutel tot de overgangstemperatuur ligt bij de interactie die zorgt dat de elektronen een paar vormen. Voor de grote groep supergeleiders met een lage overgangstemperatuur is bekend wat deze interactie is. Het is theoretisch echter niet mogelijk met deze interactie overgangstemperaturen te halen boven de -240°C. De interactie die het mogelijk maakt deze grens

te overschreiden in hoge temperatuur supergeleiders is vooralsnog niet begrepen. Een goed begrip hiervan zou mogelijkerwijs nieuwe materialen met nog hogere overgangstemperaturen op kunnen leveren. Voor een bepaalde samenstelling van een hoge temperatuur supergeleider is er boven T_c een soort overgangstoestand, die in normale supergeleiders niet bestaat. Deze overgangstoestand, of pseudogap phase, zou de ontbrekende informatie over de paarvormings-interactie kunnen leveren.

In het masterproject waar dit het verslag van is, is geprobeerd door middel van warmtebehandelingen het materiaal $(Pb,Bi)_2Sr_2CaCu_2O_{8+\delta}$ in deze overgangstoestand te krijgen. Door middel van susceptibiliteits-, weerstands- en fotoemissie metingen is vervolgens onderzocht of de toestand daardwerkelijk is bereikt. Met een hoge waarschijnlijkheid is dit echter bij geen enkele toegepaste warmtebehandeling gelukt. Dit betekent dat de tot dusver gebruikte methode niet toereikend is.

Het voornaamste deel van het onderzoek betrof de weerstandsmetingen. Het bleek dat het maken van een stabiel en goed geleidend elektrisch contact met het materiaal moeilijker was dan gedacht. Veelal lieten de contacten bij lage temperaturen (-250°C) los, of was de weerstand na enkele dagen te hoog geworden om nog metingen te verrichten. Uiteindelijk is een methode van contacten maken gevonden, waarbij de grootste problemen opgelost zijn. Goud wordt hierbij opgedampt op de hoekpunten van het materiaal en met zilverpasta wordt dit verbonden aan koperdraden. Na toepassing van eventuele andere technieken om de juiste structuur te krijgen, kan met deze methode van contacten maken relatief snel (enkele dagen) worden nagegaan of inderdaad de overgangstoestand bereikt is.

8   Acknowledgements

A   Gauge Invariance

This section will discuss the gauge invariance of a vector potential and accompanying scalar field. By choosing an appropriate gauge transformation, equations can become much more attractive and easier in use, for instance in equation (36) the scalar field can be dropped due to a gauge transformation. The vector potential is defined by:

$$\mathbf{B} = \nabla \times \mathbf{A} \tag{57}$$

which, combined with Faraday's law

$$\nabla \times \mathbf{E} = -\frac{\partial \mathbf{B}}{\partial t} \tag{58}$$

leads to the following equation for the electric field

$$\nabla \times (\mathbf{E} + \frac{\partial \mathbf{A}}{\partial t}) = 0 \tag{59}$$

Since the rotation of the gradient of a scalar field is equal to zero ($\nabla \times (\nabla V) = 0$), equation (59) can be rewritten as follows

$$E = -\nabla V - \frac{\partial \mathbf{A}}{\partial t} \tag{60}$$

If a certain potential is invariant under a transformation, there exist two sets of potentials, (V, $\mathbf{A}$) and (V', $\mathbf{A}'$), which correspond to the same electric and magnetic field. The latter potential can be written as:

$$\mathbf{A}' = \mathbf{A} + \boldsymbol{\alpha} \tag{61}$$
$$V' = V + \beta, \tag{62}$$

If both potentials have the same electric and magnetic field, the superimposed vector and scalar field $\boldsymbol{\alpha}$ and β should have no effect on the magnetic and electric field. From equations (57) and (60) the following relations can thus be obtained:

$$\nabla \times \boldsymbol{\alpha} = 0 \tag{63}$$
$$-\nabla \beta - \frac{\partial \boldsymbol{\alpha}}{\partial t} = 0 \tag{64}$$

Noting again that the rotation of the gradient of a scalar field is zero, these two equations reduce to:

$$\nabla(\beta + \frac{\partial \lambda}{\partial t}) = 0 \tag{65}$$

where λ is defined by $\boldsymbol{\alpha} = \nabla \lambda$. The term in parenthesis is thus constant in space, but could depend on time. This time dependent factor, say $f(t)$, can

however be absorbed in λ by defining a new λ to which $\int_0^t f(t')dt'$ is added. Therefore it follows that the transformation:

$$\mathbf{A}' = \mathbf{A} + \nabla\lambda \tag{66}$$

$$V' = V - \frac{\partial\lambda}{\partial t} \tag{67}$$

gives the same electric and magnetic field. All one has to do is find the right scalar field λ.

In the particular case of equation (36), the classical Hamiltonian in the presence of an electromagnetic field is given by:

$$H = \frac{1}{2m}(\mathbf{p} - q\mathbf{A})^2 + qV \tag{68}$$

where q is the charge that generates the electromagnetic field (for electrons $q = \frac{e}{c}$). If one would choose the gauge $\lambda = Vt$,

$$\mathbf{A}' = \mathbf{A} + \nabla Vt \tag{69}$$

$$V' = 0 \tag{70}$$

and the Hamiltonian reduces to (36) where $\mathbf{A}'$ is written as $\mathbf{A}$.

B   Reliability of resistivity measurements

Although the principle of the MagLab is quite straightforward, the device itself is more a black box. A sample is placed in the machine and a number for the resistance of a certain orientation is obtained. A test measurement with a copper wire (figure 16) seemed to indicate that the values obtained are close to literature values and therefore reliable. Measurements of several months later however introduced some doubts about the reliability of the resistivity measurements. Figure 42 for instance shows two measurements on the same, approximately square sample. The difference between the two
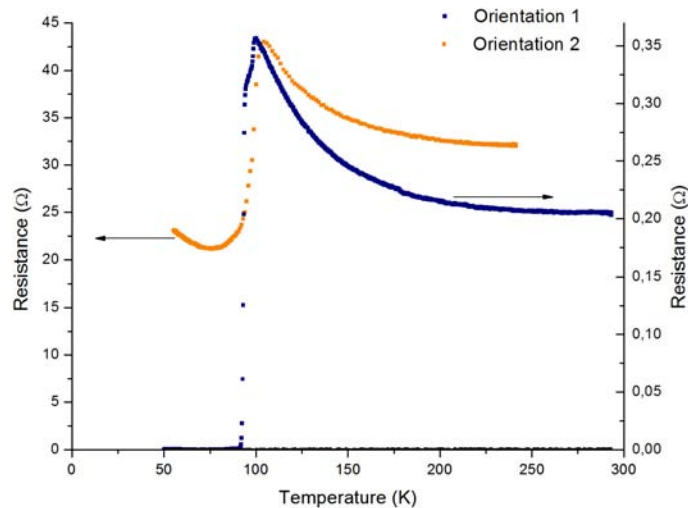

Figure 42: Two measurement of one sample, annealed 24 hours in vacuum at 450°C and 100 hours in nitrogen at 700°C. The difference is a 90 degrees rotation of the voltage and current contacts. While the sample is approximately square and the ab-plane resistivity nearly isotropic, a factor of about 120 difference is observed between the geometries.

measurements is a 90 degrees rotation of the voltage and current contacts. This rotation is done by switching external cables to probe a different side of the square sample holder (the contacts used are the same, only a current contact is turned into a voltage contact and vice versa). Therefore, the sample does not have to be taken out of the MagLab and the conditions are exactly the same for both measurements. For a square sample with isotropic ab-plane resistivity it is then very suspicious that there is a big difference between the two resistances.

Since the out-of-phase signal is zero and no considerable noise is detected at the low current applied, the unexpected difference in resistances is not due to poor contacts, but is likely to have been caused by a connection somewhere in the MagLab. To test these suspicions, a piece of solder of a few centimeters was attached to one side of the sample holder and the room temperature resistance was measured. A value in the range of several mΩ is expected from literature. For the orientation in which the measurement with a small resistance was measured of figure 42, this was indeed the case. The other orientation had however 1000 times larger resistance. The two remaining sample holder orientations, which can be probed by using a different plug did not give a response at all. This may be taken as evidence that a connection inside the MagLab is malfunctioning. The fact that the reference measurement mentioned in section 4.2 gave a result close to literature values, might therefore be a 'lucky hit' since only one sample orientation was measured.

Resetting the entire system and repeating the measurements suddenly gave the expected resistance in both orientations. Over time, one or more connections inside the system might have deteriorated. Where this bad connection is located, can be determined by a rigorous examination of the system. Unfortunately this was not done during the time span of this project.

C Angular distortion corrector

To correct for angular distortions, due, for instance, to misalignment of the sample pocket or a slightly tilted sample, a program has been written in Igor, the software used for data analysis. Figure 43 shows an image of the program panel. The program prompts for a Fermi surface map and the polar and azimuthal values of the fitted peak-intensities. Both Fermi surface map and peak intensity fits are plotted in k-space using formulas (53) and (54). Change of any of the parameters in the formulas will automatically update the image. The fitted peak-intensities are also shown in a separate graph, where the peaks in the Y-quadrant are plotted on top of those in the X-quadrant. A third and fourth data set in the lower right graphic is obtained by mirroring the original data points in the ΓY- and ΓX-line. For
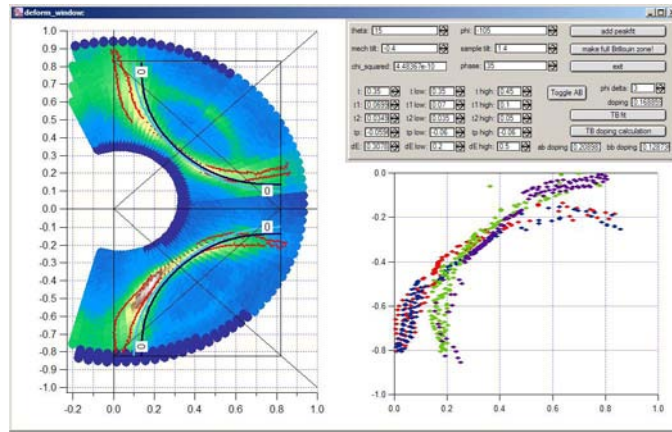

Figure 43: Image of the program panel. The left figure shows the measured band structure in k-space. On the right, the fitted peak-intensities are plotted on top of each other together with their mirror images.

a perfectly symmetric band structure, all four curves should fall on top of each other. By manually adjusting the parameters, a minimal least square value (χ) can be found. The bands should not only be symmetric, but the midpoint of the main- and shadow band along the ΓY-direction should also be precisely at $(\frac{\pi}{2}, \frac{\pi}{2})$. Once this requirement is met, fitted peak-intensities of a second constant energy map (MDM) can be loaded. With the peak-intensities of the two energy values, a tight binding fit can be made. Since mainly the bonding band is resolved, $t_\perp$ is kept at negative values. All other fitting parameters are kept within the range of literature values. After fitting, the doping concentration can be calculated by integrating the Fermi surface area and using equation (52). This is done for both the bonding- and anti-bonding band. The average of the two doping levels gives the hole doping concentration per Cu atom.

D   Beamtimes

Part of the research work in the quantum electron matter group are the beamtimes at synchrotrons in Germany and Switzerland. During this project, a total of two weeks were spent at the SLS near Villigen and three weeks at BESSY in Berlin, spread out over a total of four separate beamtimes. Most of this time was dedicated to the study of LSMO, a giant magneto resistance material, of which analysis is being carried out by Sanne de Jong. A small part of the beamtime was reserved to search for the pseudogap of Bi-2212 at the M-point and study the renormalization due to coupling to a bosonic mode, data which is being analyzed by Iman Santoso. Despite the fact that few of the measurements had a direct impact on the masters project, it was a great experience to take part in the beamtimes. Besides driving to and from the respective synchrotrons, a lot of experience was gained in measuring and many aspects necessary for a measurement, for instance the alignment of the experimental setup to the beamline.

At a synchrotron, electrons are accelerated in a circular motion close to the speed of light. If these electrons are guided through an alternating magnetic field, or undulator, they will release the extra energy thus gained in the form of light[17]. The required energy of the light can subsequently be selected by a monochromator. Therefore, light of any energy between a few eV and tens of keV can be used for experiments. For photoemission, typically energies from a few to about a hundred eV are used. At higher energies, core levels are probed which are not the focus of the research described here. So a wide range of energies can be selected with a high intensity and small focus, which make the synchrotron ideal for angle resolved photoemission, all the more because of the energy dependence of ionization cross section.

Before a measurement can be performed however, the spectrometer has to be connected to the beamline and ultra high vacuum has to be reached, just like has been done with the FAMoS. This can be done by an intricate pumping system and by baking the entire system with heating tapes to more than a hundred degrees Celcius to outgas all parts. To ensure uniform temperature distribution over the system, aluminium foil is used to cover the entire setup. When the proper pressure is achieved (10^{-10} mbar), the spectrometer should be aligned perfectly to the incoming beam. Proper alignment means that the electrons that are emitted perpendicularly from the sample fall onto the center of the detector and as much electrons as possible are emitted and detected. Using set screws at three corners of the setup, the height can be adjusted in order to have the beam and analyzer in the same

---

[17]Any non straight motion will force the relativistic electrons to emit light, also the circular motion in the synchrotron itself. The undulator merely enables a controlled light emission.

Figure 44: Picture of the U125-beamline at BESSY and the ARPES setup.

plane. Subsequent corrections in position are performed by gently tapping the legs with rubber hammers. Since the light spot has a diameter of only a millimeter, minor adjustments can already lead to huge changes in emission, making alignment a time consuming and precise venture. One of my main achievements during one of the beamtimes was to assist in getting the system ready for use, especially with the alignment. Not only is it nice, and if successful satisfactory, to prepare the system, but during the task many aspects of the machine and auxiliaries become known that would otherwise be overlooked in routine use. Figure 44 shows the system at BESSY after successful alignment.

References

[1] http://www.wikipedia.org

[2] http://superconductors.org

[3] http://physics.nist.gov

[4] http://es1.ph.man.ac.uk/research/facilities/IntroHDA.pdf

[5] http://fy.chalmers.se/ yurgens/ijj.html#CooperGray

[6] L.H. van der Pauw, *A method of measuring the resistivity and Hall coefficient on lamellae of arbitrary shape*, Philips Technical Review **20**, 220-224 (1958)

[7] H.C. Montgomery, *Method for measuring electrical resistivity of anisotropic materials*, Journal of Applied Physics **42**, number 7, 2971-2975 (1971)

[8] Logan et al., *Series for computing current flow in a rectangular block*, Journal of Applied Physics **42**, number 7, 2975 (1971)

[9] J.D. Wasscher, , Philips Research Reports **16**, 301 (1961)

[10] A.Damascelli, *Probing the electronic structure of complex systems by ARPES*, Physica Scripta **T109**, 61-74 (2004)

[11] F.Reinert et al., *Photoemission spectroscopy - from the early days to recent applications*, New Journal of Physics **7**, 97 (2005)

[12] A. Damascelli et al., *Angle-resolved photoemission studies of the cuprate superconductors*, Reviews of Modern Physics **75**, number 2, 473 (2003)

[13] A. Mans et al., *Experimental proof of a structural origin for the shadow Fermi surface of $Bi_2Sr_2CaCu_2O_{8+\delta}$*, Physical Review Letters **96**, 107007 (2006)

[14] A.A. Kordyuk et al., *Origin of the peak-dip-hump line shape in the superconducting-state $(\pi,0)$ photoemission spectra of $Bi_2Sr_2CaCu_2O_8$*, Physical Review Letters **89**, number 7, 077003-1 (2002)

[15] X.H. Chen et al., *Anisotropic resistivities of single-crystal $Bi_2Sr_2CaCu_2O_{8+\delta}$ with different oxygen content*, Physical Review B **58**, number 21, 14219 (1998)

[16] F. Rullier et al., *Disorder and transport in cuprates: weak localization and magnetic contributions*, Physical Review Letters **87**, number 15, 157001 (2001)

[17] A.I. Liechtenstein et al., *Quasiparticle bands and superconductivity in bilayer cuprates*, Physical review B **54**, number 17, 12505 (1996)

[18] Y.-D. Chuang et al., *Bilayer splitting and coherence effects in optimal and underdoped $Bi_2Sr_2CaCu_2O_{8+\delta}$*, Physical Review B **69**, 094515 (2004)

[19] N.L. Wang et al., *Temperature dependence of the in-plane resistivity in underdoped $Bi_2Sr_2CaCu_2O_y$ single crystals*, Physical Review B **54**, number 10, 7445 (1996)

[20] K.Q. Ruan et al., *The systematic study of normal-state transport properties of Bi-2212 crystals*, Journal Phys. Condens. Matter **11**, 3743 (1999)

[21] B. Leontić et al., *Reliable electrical contacts on $Bi_2Sr_2CaCu_2O_{8+\delta}$ single crystals*, Supercond. Sci. Technol. **11**, 594 (1998)

[22] S. Aukkaravittayapun et al., *Low-resistance electrical contacts to single crystal BSCCO whiskers*, Supercond. Sci. Technol. **8**, 718 (1995)

[23] S. Martin et al., *Temperature dependence of the resistivity tensor in superconducting $Bi_2Sr_{2.2}Ca_{0.8}Cu_2O_8$ crystals*, Physical Review Letters **60**, number 21, 2194 (1988)

[24] T. Motohashi et al., *Systematic decrease of resistivity anisotropy in $Bi_2Sr_2CaCu_2O_y$ by Pb doping*, Physical Review B **59**, number 21, 14080 (1999)

[25] T. Timusk et al., *The pseudogap in high-temperature superconductors: an experimental survey*, Rep. Prog. Phys. **62**, 61 (1999)

[26] J.L. Tallon and J.W. Loram, *The doping dependence of T^* - what is the real high T_c phase diagram?*, Physica C **349**, 53 (2001)

[27] J.G. Bednorz and K.A. Müller, *Possible high T_c superconductivity in the Ba-La-Cu-O system*, Z. Phys. B **64**, 189 (1986)

[28] J. Bardeen, L.N. Cooper and J.R. Schrieffer, *Theory of superconductivity*, Physical Review **108**, number 5, 1175 (1957)

[29] L.N. Cooper, *Bound electron pairs in a degenerate Fermi gas*, Physical Review **104**, number 4, 1189 (1956)

[30] F. Steglich et al., *Superconductivity in the presence of strong Pauli paramagnetism: $CeCu_2Si_2$*, Physical Review Letters **43**, number 25, 1892 (1979)

[31] B.D. Josephson, *Possible new effects in superconductive tunnelling*, Physics Letters **1**, number 7, 251 (1962)

[32] V. Arpiainen and M. Lindroos, *Effect of symmetry distortions on photoelectron selection rules and spectra of $Bi_2Sr_2CaCu_2O_{8+\delta}$*, Physical Review Letters **97**, 037601 (2006)

[33] A.A. Kordyuk et al., *Doping dependence of the Fermi surface in $(Bi,Pb)_2Sr_2CaCu_2O_{8+\delta}$*, Physical Review B **66**, 014502 (2002)

[34] J. Mesot et al., *Superconducting gap anisotropy and quasiparticle interactions: a doping dependent photoemission study*, Physical Review Letters **83**, number 4, 840 (1999)

[35] S.V. Borisenko et al., *Superconducting gap in the presence of bilayer splitting in underdoped $(Pb,Bi)_2Sr_2CaCu_2O_{8+\delta}$*, Physical Review B **66**, 140509(R) (2002)

[36] Jörg Fink et al., *Dressing of the charge carriers in high-T_c superconductors*, cond-mat 0512307, May 2006

[37] R.A. Serway, *Principles of physics*, 2nd edition, page 602, Saunders College Pub. London, (1998)

[38] C.P. Poole, H.A. Farach and R.J. Creswick, *Superconductivity*, Academic Press, 1995, ISBN:0-12-561456-X

[39] S. de Jong, *On the aging of $(Pb,Bi)_2Sr_2CaCu_2)_{8+\delta}$*, masters thesis chemistry, University of Amsterdam, 26 Januari 2006

[40] M. McElfresh, Shi Li and Ron Sager, *Effects of magnetic field uniformity on the measurement of superconducting samples*, Quantum Design, San Diego

[41] MagLabExa user manual, Oxford Instruments Superconductivity Limited, Abingdon, 2000